AUTHOR QUERY FORM

ELSEVIER	**Journal: JAES** **Article Number: 666**	**Please e-mail or fax your responses and any corrections to:** **E-mail: corrections.esch@elsevier.sps.co.in** **Fax: +31 2048 52799**

Dear Author,

Any queries or remarks that have arisen during the processing of your manuscript are listed below and highlighted by flags in the proof. Please check your proof carefully and mark all corrections at the appropriate place in the proof (e.g., by using on-screen annotation in the PDF file) or compile them in a separate list.

For correction or revision of any artwork, please consult http://www.elsevier.com/artworkinstructions.

Articles in Special Issues: Please ensure that the words 'this issue' are added (in the list and text) to any references to other articles in this Special Issue.

Uncited references: References that occur in the reference list but not in the text – please position each reference in the text or delete it from the list.

Missing references: References listed below were noted in the text but are missing from the reference list – please make the list complete or remove the references from the text.

Location in article	Query / remark Please insert your reply or correction at the corresponding line in the proof
Q1	This section comprises references that occur in the reference list but not in the body of the text. Please position each reference in the text or, alternatively, delete it. Any reference not dealt with will be retained in this section.
Q2	Reference "Annen et al. (2006) is cited in the text but not listed. Please check.

delete the ref.

Added to the list

Electronic file usage

Sometimes we are unable to process the electronic file of your article and/or artwork. If this is the case, we have proceeded by:

☐ Scanning (parts of) your article   ☐ Rekeying (parts of) your article   ☐ Scanning the artwork

Thank you for your assistance.

Petrologic and geochemical constraints on the origin of Astaneh pluton, Zagros orogenic belt, Iran

Zahra Tahmasbi [a], Antonio Castro [b,*], Mahmud Khalili [c], A. Ahmadi Khalaji [d], Jesús de la Rosa [b]

[a] Department of Mine, Faculty of Engineering, University of Lorestan, Khorramabad, Iran
[b] Department of Geology, University of Huelva, Campus del Carmen, 21071 Huelva, Spain
[c] Department of Geology, Faculty of Science, University of Isfahan, Isfahan, Iran
[d] Department of Geology, Faculty of Science, University of Lorestan, Lorestan, Iran

ARTICLE INFO

ABSTRACT

The Astaneh plutonic complex consists of a series of granitoid rocks ranging in composition from quartz-diorites to monzogranites and evolving from metaluminous to weakly peraluminous compositions. They belong to the high-K calc-alkaline series, having features of typical Andean-type cordilleran granitoids. Trace and rare-earth elements distribution patterns for the Astaneh rocks indicate a distinctive depletion in Nb, Sr, Ba, P and Ti relative to other trace elements and a greater enrichment in LILE compared to HFSE. These geochemical characteristics suggest the participation of an important recycled (sedimentary?) component in the source region of the granitoids. They have Sr initial isotopic ratios in the range 0.7078–0.7084 and negative ε_{Nd} values of −5.39 to −6.13 for a time of generation of 170 Ma. There is a genetic link between quartz-diorites and granodiorites, the dominant rock types of the Astabeh intrusion. Direct melting or fractionation from a diorite source is very unlike. It is proposed that the Astaneh parental Qtd-diorite magmas were produced by the partial melting of a mixed source, dominantly composed of amphibolites and sediments, that was formed during subduction of Neo-Tethyan oceanic crust below the Iranian microcontinent during Middle Jurassic times.

© 2010 Elsevier Ltd. All rights reserved.

1. Introduction

The Zagros orogenic belt resulted form the collision between the Arabia and Eurasia plates (Sengor, 1992; Alavi, 1994, 2007; Agard et al., 2005). It belongs to the large Alpine–Himalayan mountain chain, also referred to as the Tethysides orogenic belt (Sengor, 1987). In contrast with other sector of this huge collisional belt, the Zagros system is characterized for a long-lived magmatic activity developed along more than 150 Ma from the Mesozoic to the Plio-Quaternary (Omrani et al., 2008). This long-lived magmatic activity is widespread along two well-defined linear belts, namely the Sanandaj–Sirjan magmatic belt (SSMB) and the Urumieh–Dokhtar magmatic assemblage (UDMA), following the zonal division modified by Alavi (2007). Most of the magmatic rocks developed from the beginning of subduction at the Jurassic (Arvin et al., 2007) up to the collision-related magmatism with climax at the Eocene times (Mazhari et al., 2009; Omrani et al., 2008), have a common calc-alkaline affinity with geochemical and petrological features similar to those of Andean-type magmatism (Berberian et al., 1982). However, some alkaline (Mazhari et al., 2009) and shoshonitic magmas (Amidi et al., 1984) are associated in space

and time with calc-alkaline batholiths and their extrusive equivalents. These have been described in both the SSMB and the UDMA, denoting the igneous complexity of the Zagros system (Ghalamghash et al., in press) that resulted from a complex plate convergence process (Alavi, 2007).

Some recent studies on the volcanic rocks in these two magmatic arcs (Omrani et al., 2008) revealed interesting data about the relation of magmatism and plate convergence in this region. The presence of two magmatic arcs separated in space and time, containing a wide variety of igneous rock series, makes the Zagros convergence system one of great interest to test petrogenetic models related to subduction and arc magma generation. Large plutonic bodies, still poorly known, are associated with volcanic rocks in both magmatic belts, SSMB and UDMA. One of these plutonic complexes is the Astaneh intrusion studied in detail here for the first time. It forms part of a linear belt of plutons distributed along the SSMB. Most of these plutonic associations display a varied spectrum of rocks from gabbros to granites, typical of active continental margins. Although the relation with a subducting slab is clear for the tectonic environment, the processes of magma production remains controversial. Whether granites represent fractionates from a parental mantle-derived diorite or gabbro or, by contrast, they are crustal melts produced from a mafic source is a matter of sample debate in calc-alkaline associations.

* Corresponding author.
  E-mail address: dorado@uhu.es (A. Castro).

The aim of this paper is to use geochemical features jointly with field and petrographic relations to determine the origin of magmas and tectonic environment for magma generation. The results of this study may help to understand the complex magmatic evolution of active margins in relation with subduction and collision. These results will shed light on this period of the Mesozoic history in Iran, an area for which little information has been available so far.

2. Geological setting

From Late Precambrian until Late Paleozoic, South Eastern Turkey, Central Iran, Central Afghanistan, Southern Pamir and Arabia were part of the Gondwana supercontinent. This was separated from the Eurasian plate by the Hercynian Ocean called Paleotethys. During Middle to Late Triassic, coeval with the closure of the Paleotethys in the north, a rifting episode along the Zagros belt
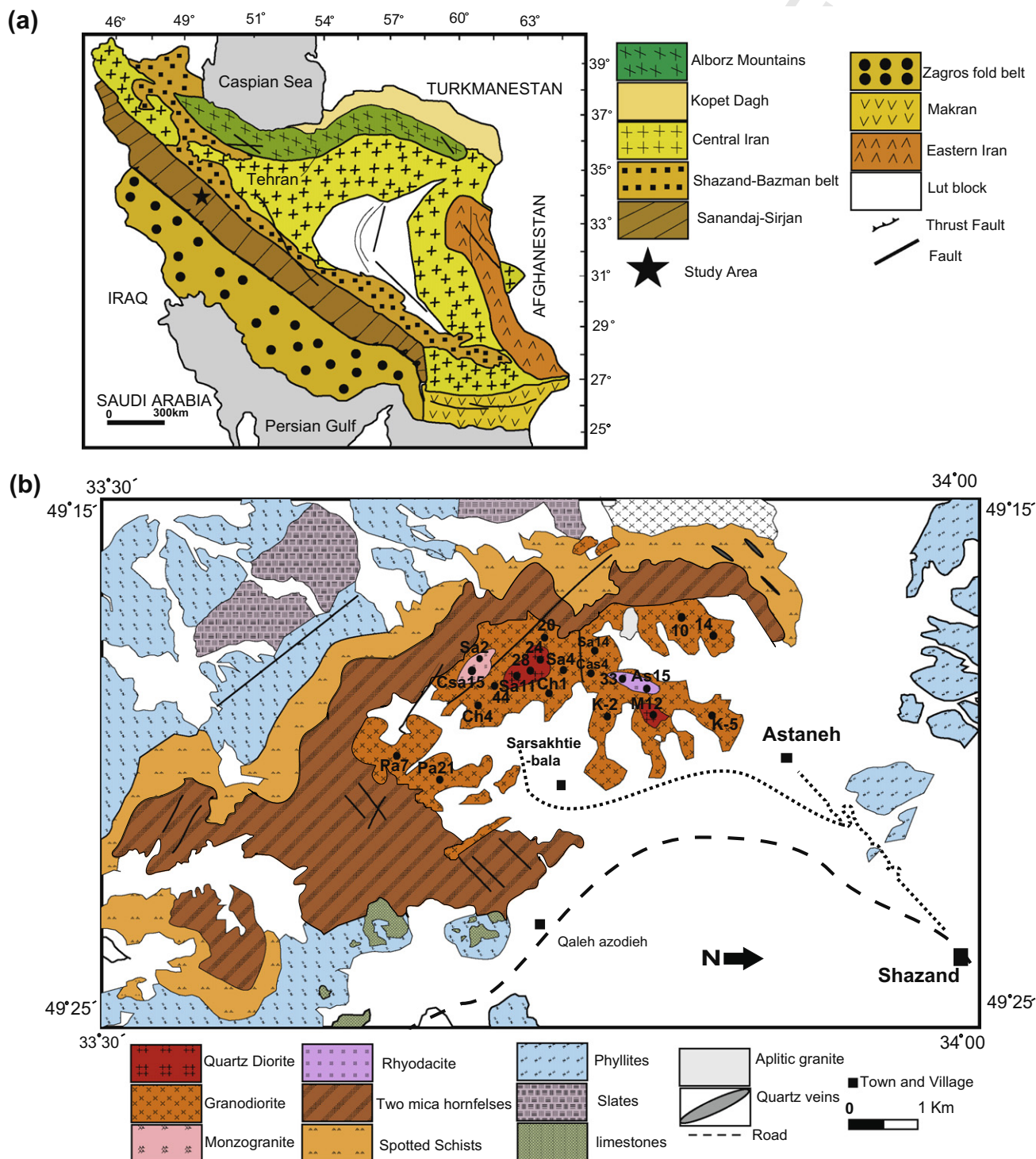

Fig. 1. Geological map of the Astaneh intrusion and location of analyzed samples. Inset shows the location of the Astaneh area in the Iran geological map (modified from: Stöcklin and Setudinia (1972)).

resulted in the opening of a new ocean called Neo-tethys. Closure of Paleotethys resulted in the subduction of the oceanic crust of the Neo-tethys beneath the Eurasian plate during Triassic–Jurassic time. Subduction inception dates back to the Late Triassic–Early Jurassic (Berberian and Berberian, 1981; Arvin et al., 2007). This led to an Early Cimmerian metamorphic event, recorded in the southwest Sanandaj–Sirjan Zone (Berberian and King, 1981; Berberian and Berberian, 1981; Hooper et al., 1994) associated with Upper Triassic emplacement of intrusive bodies (Sabzehei, 1994; Berberian and Berberian, 1981) within this zone. Closure of the oceanic domain was marked by the obduction of ophiolites along the main Zagros thrust (MZT) in the late cretaceous (Agard et al., 2005). Finally, the closure of the Neo-tethys and collision of Arabia and Central Iran took place during the Neogene times (Berberian and Berberian, 1981).

The Sanandaj–Sirjan magmatic belt (SSMB), in which is the Astaneh pluton is located, is a 150–200 km wide zone extending from northwest to southeast Iran (Fig. 1a). This tectonic-magmatic zone has undergone various metamorphic episodes during the subduction of the Tethyan Ocean under the Iranian block, obduction of ophiolites along the MZT and, finally, continental collision (Stöcklin, 1968).

According to Mohajjel et al. (2003), major structures in the Sanandaj–Sirjan Zone formed during three separate major events: (1) Subduction along the active margin of Central Iran, at the northeastern margin of the Tethys. (2) Ophiolite obduction along the northeastern margin of the Tethys. (3) Continental collision of the Arabia and Central Iran.

Subduction of the Tethys Ocean is the most important event in the construction of the SSMB. Intense folding with south–southwest vergence and low-grade metamorphism are associated with this subduction event. Accordingly, Berberian (1983) considered this zone as a Mesozoic magmatic arc, and a Tertiary fore-arc. The presence of a narrow arc-trench gap in this belt is an indication of steep subduction (Isacks and Barazangi, 1977; Berberian and Berberian, 1981). It has been suggested that the Sanandaj–Sirjan calc-alkaline magmatic arc, including the Astaneh pluton, developed over a high angle subducting oceanic slab in the Neo-tethyan subduction zone from Late Triassic to Late Cretaceous times (e.g. Berberian and Berberian, 1981; Shahabpour, 2005).

The second important constructing event in this zone is ophiolite obduction along the northeastern margin of the Tethys, including the Neyriz and Kermanshah ophiolites, which indicate obduction of oceanic fragments along the Zagros suture.

Finally, the third important event is the continental collision of Arabia against Central Iran at the Miocene. This deeply affected this zone reaching a climax after opening of the Red Sea and the Gulf of Aden (Mohajjel et al., 2003). Some age determinations have been reported in the SSMZ (Sabzehei et al., 1970; Valizadeh and Cantagrel, 1975; Ahmadi-Khalaji et al., 2007; Arvin et al., 2007).

3. Geology of the Astaneh pluton

The Astaneh pluton is a NNW–SSE trending body covering an area of 30 km² (approximately 10 km length and 3 km width; Fig. 1b). It is intrusive into low-grade metamorphic rocks such as slates, phyllites and schists (Ahmadi Khalaji, 2006). The whole area is characterized by metamorphic rocks of Jurassic age (Baharifar, 2004) and by the presence of the intrusive rocks that form the Astaneh pluton. The intrusion of the Astaneh pluton produced a contact metamorphism at the albite-epidote hornfels facies. Frequent lithologies are spotted schist, hornfels schist and hornfelses (Ahmadi Khalaji, 2006).

Upper Cretaceous ages were reported for the Astaneh intrusion (ca. 99 Ma; Rb–Sr data; Masoudi, 1997; Masoudi et al., 2002). However, precise U–Pb single zircon dating (Ahmadi Khalaji, 2006), carried out on a VG sector 354 mass spectrometer at the Massachusetts Institute of Technology (USA) for six different granitoids of the region, including a sample of the Astaneh granodiorite (170.7 ± 1 Ma), indicate a short-lived episode of magmatic activity during the period 172–169 Ma. Accordingly, a reference age of 170 Ma is used in this study for isotope initial ratio calculations.

The composition of the pluton ranges from quartz-diorite to monzogranite. Abundant subvolcanic rocks of dacite composition are also included as part of the same magmatic cycle. Tonalites and more basic rocks are included as large enclaves. A common feature of Sanandaj–Sirjan Zone granitic intrusions is the conspicuous presence of mafic microgranular enclaves, particularly well represented in the granodiorites and monzogranites of Astaneh.

The studied rocks in the Astaneh pluton include: (1) quartz-diorites, (2) granodiorites, (3) monzogranites, (4) microgranular enclaves, and (5) a small dacitic body of 3 km diameter.

Qtz-diorites occur as minor irregular bodies at the centre and southern areas of the intrusion. They are surrounded by granodiorites with which they show gradual boundaries. The grain size is homogeneous (2–3 mm). Granodiorites are the most abundant rocks in the pluton. They are medium to coarse-grained rocks (2.5 mm, ranging from 0.7 to 5.6 mm) in which mica and amphibole, are conspicuous phases. Monzogranites are abundant at the southern area of the pluton (Fig. 1b). They are characterized by homogeneous textures and mineralogy. They may form patches within the granodiorites, with which they have transitional boundaries. These rocks are light colored and fine to coarse-grained (3.1 mm, ranging from 1.7 up to 7 mm).

Mafic microgranular enclaves are normally found enclosed in granodiorites and monzogranites. They are oval bodies and irregularly shaped blobs, ranging in size from mm to meters. Enclaves show sharp boundaries with the host granodiorite or monzogranite.

A small stock-like body of semicircular morphology (about 3 km diameter), described here as "dacite stock", outcrops at NE of the study area. It is composed of subvolcanic rocks of dacitic composition. They may represent possibly the subvolcanic equivalent of the pluton and, thus, they were also sampled for geochemical analyses.

4. Sampling and analytical methods

A total of about 300 samples from different facies, including quartz-diorite, granodiorite, monzogranite, enclaves and dacites were collected. Two hundred thin sections of these samples were prepared and studied by optical microscope and 40 thin polished sections were selected for electron microscopy and microprobe analyses. Representative samples (35 samples) were selected for whole rock geochemistry. Sample weights were 1–1.5 kg before crushing and powdering. This amount is enough due to the homogeneity and the medium (2–4 mm) to fine (<2 mm) grain size of the selected samples. Major elements and Zr were analyzed by X-ray fluorescence (XRF) at the University of Oviedo (Spain) using glass beads. Precision of the XRF technique was better than ±1.5% relative. Trace element and rare-earth elements (REE) were analyzed by inductively coupled plasma mass spectrometry (ICP-MS) with an HP-4500 system at the University of Huelva, following digestion in a $HF + HNO_3$ (8:3) solution, drying and second dissolution in 3 ml HNO_3. The average precision and accuracy for most of the elements were controlled by repeated analyses of SARM-1 (granite) and SARM-4 (norite) international rock standards. They fall in the range of 5–10% relative. The results of the analyses are reported in Table 1.

The compositions of the minerals were determined by electron microprobe analysis of polished thin sections. The analyses were

Table 1
Whole rock compositions of the Astaneh intrusion.

Sample	Sa11	24	28	As5	M12	CSa25	14	Sa4	44	Sa14	K5	K2	CSa25	20
Lithology	QD	QD	QD	QD	QD	QD	GD	GD	GD	GD	GD	GD	GD	GD
SiO_2	57.74	61.54	61.65	62.01	62.62	63.59	63.02	63.03	63.09	63.29	63.36	63.57	63.59	63.76
TiO_2	0.59	0.53	0.59	0.54	0.49	0.52	0.53	0.53	0.54	0.56	0.55	0.54	0.52	0.52
Al_2O_3	16.61	16.40	16.58	16.80	16.12	16.00	16.10	16.10	16.41	16.01	15.09	16.02	16.00	15.99
FeOt(1)	7.23	6.06	6.25	5.53	5.34	5.13	5.81	5.41	5.36	5.75	5.76	5.56	5.13	5.33
MgO	4.55	3.49	3.38	2.86	2.89	2.46	3.09	2.82	2.86	2.90	2.96	2.86	2.46	2.81
MnO	0.17	0.13	0.12	0.12	0.12	0.10	0.12	0.11	0.11	0.11	0.12	0.11	0.10	0.11
CaO	6.63	5.22	5.12	5.16	3.92	4.30	4.75	4.98	4.83	4.73	4.62	4.61	4.30	4.60
Na_2O	2.59	2.71	2.43	2.58	2.83	2.63	2.47	2.40	2.54	2.41	2.43	2.48	2.63	2.66
K_2O	2.02	2.47	2.53	2.40	2.84	3.03	2.59	2.66	2.39	2.83	2.89	2.51	3.03	2.50
P_2O_5	0.08	0.11	0.11	0.11	0.08	0.11	0.10	0.10	0.10	0.12	0.11	0.11	0.11	0.1
LOI	1.46	1.47	1.11	1.26	2.62	1.54	1.42	1.13	1.60	1.14	1.37	1.58	1.54	1.66
Total	99.7	100.1	99.9	99.4	99.9	99.4	100.0	99.3	99.8	99.9	99.3	99.9	99.4	100.1
Mg# (2)	0.53	0.51	0.49	0.48	0.49	0.46	0.49	0.48	0.49	0.47	0.48	0.48	0.46	0.46
ASI (3)	0.90	0.99	1.03	1.04	1.09	1.04	1.04	1.01	1.06	1.02	0.97	1.06	1.04	1.04
Trace elements (ppm)														
Li	55.2	32.8	29.8	60.4	58.1	54.4	31.0	53.5	41.1	64.8	51.2	53.8	54.4	44.1
Be	1.5	1.0	1.4	1.9	1.5	1.6	1.2	1.8	1.6	1.7	1.4	1.3	1.6	1.3
Cr	146	90.7	78.3	151	62.4	144	96.2	166	171	200	153	110	144	114
Co	20.5	10.5	14.0	15.7	9.34	11.8	11.1	17.0	13.0	18.5	13.2	24.1	11.8	24.1
Ni	21.1	10.5	16.2	17.1	15.1	12.7	14.5	19.5	14.8	21.3	13.2	14.1	12.7	14.6
Rb	87.4	74.7	86.3	95.7	91.5	95.3	70.4	101	79.5	108	97.3	82.8	95.3	80.2
Sr	142	123	141	160	128	144	124	153	153	151	136	139	144	147
Y	42.0	11.9	16.9	17.7	14.3	17.7	17.7	22.1	16.9	24.6	19.9	16.6	17.7	18.0
Zr	63.1	96.6	91.9	97.3	89.2	103	103	104	117	104	110	104	116	362
Nb	11.1	6.77	8.52	9.82	7.81	8.54	8.18	10.5	8.79	11.7	8.68	8.92	8.54	8.67
Cs	10.6	6.46	6.16	14.0	11.9	8.22	7.03	9.23	12.8	12.6	9.48	10.7	8.22	9.01
Ba	162	204	286	292	230	284	206	268	247	284	261	257	284	262
La	29.8	12.1	15.4	20.6	19.0	23.8	17.9	26.4	22.4	34.3	14.0	14.2	23.8	23.7
Ce	65.3	26.0	32.6	41.5	38.5	49.6	36.9	51.1	45.8	63.6	31.5	29.3	49.6	46.5
Pr	9.78	3.17	4.17	5.11	4.55	6.01	4.76	6.58	5.44	8.25	4.13	3.77	6.01	5.76
Nd	33.7	11.6	15.6	18.7	16.0	20.9	16.1	21.2	19.2	25.7	16.2	12.9	20.9	18.8
Sm	7.92	2.46	3.49	3.84	3.11	4.10	3.52	4.47	3.73	5.04	3.70	2.88	4.10	3.82
Eu	0.87	0.47	0.80	0.94	0.63	0.77	0.67	0.94	0.77	0.98	0.77	0.74	0.77	0.86
Gd	7.77	2.25	3.32	3.59	2.83	3.74	3.56	4.36	3.32	4.84	3.72	2.99	3.74	3.49
Tb	1.62	0.39	0.58	0.63	0.51	0.62	0.69	0.83	0.58	0.94	0.66	0.57	0.62	0.70
Dy	8.48	2.48	3.55	3.75	3.00	3.68	3.49	4.19	3.50	4.65	4.09	2.96	3.68	3.48
Ho	2.08	0.49	0.72	0.77	0.61	0.74	0.85	0.97	0.69	1.13	0.84	0.74	0.74	0.83
Er	5.27	1.33	1.98	2.01	1.72	2.00	2.16	2.49	1.95	2.87	2.35	1.88	2.00	2.06
Tm	0.88	0.20	0.29	0.30	0.25	0.30	0.35	0.40	0.27	0.46	0.33	0.30	0.30	0.35
Yb	4.86	1.32	1.83	1.87	1.67	1.93	1.93	2.20	1.83	2.60	2.24	1.70	1.93	1.96
Lu	0.83	0.19	0.26	0.28	0.24	0.27	0.33	0.39	0.27	0.46	0.34	0.30	0.27	0.33
Hf	1.26	1.82	2.57	1.96	1.76	1.70	0.54	0.71	3.94	0.82	4.24	1.09	1.70	1.22
Ta	1.44	3.31	1.24	2.53	1.64	1.80	0.84	1.00	1.76	1.31	1.73	0.85	1.80	0.88
W	4.29	4.43	1.05	8.05	0.92	8.10	3.51	7.23	9.38	10.2	8.60	5.20	8.10	5.14
Pb	15.6	9.43	18.5	31.6	20.9	16.9	11.8	15.4	153	15.4	14.6	24.7	16.9	27.1
Th	14.5	5.35	9.03	9.34	8.58	12.1	8.11	11.2	11.8	17.3	11.9	7.96	12.1	10.9
U	1.95	1.05	1.55	1.96	1.39	2.50	2.01	2.35	2.30	2.65	3.70	2.37	2.50	1.75
Ce^N/Yb^N	3.53	5.17	4.67	5.83	6.04	6.74	5.02	6.11	6.58	6.43	3.68	4.53	6.74	6.24

Sample	Ch4	10	Ch1	Pa7	Pa21	Sa2	CSa15	EK4	E25	CESa4	EPa1	E17
Lithology	GD	GD	GD	GD	GD	MZG	MZG	EHMg	EHMg	EHMg	EHMg	EHMg
SiO_2	64.07	64.20	64.50	65.14	65.53	69.16	70.05	52.63	53.82	54.35	54.57	56.09
TiO_2	0.54	0.54	0.54	0.47	0.43	0.31	0.30	0.56	0.48	0.45	0.41	0.45
Al_2O_3	15.83	16.17	15.90	15.64	15.57	15.07	15.07	14.66	15.12	13.98	14.97	14.66	15.65
FeOt	5.43	5.49	5.55	4.96	4.69	3.25	3.29	9.56	9.31	8.24	9.40	7.12
MgO	2.66	2.79	2.81	2.66	2.27	1.41	1.45	7.08	7.83	6.98	7.28	6.33
MnO	0.11	0.11	0.11	0.09	0.11	0.06	0.06	0.25	0.23	0.23	0.27	0.17
CaO	4.11	4.72	3.98	4.80	3.88	2.72	2.80	8.95	9.49	8.53	8.12	8.02
Na_2O	2.49	2.42	2.45	2.42	2.56	2.74	2.79	2.67	2.15	2.52	2.06	2.72
K_2O	2.70	2.57	2.55	2.74	3.23	4.17	3.71	1.37	1.32	1.69	1.27	1.68
P_2O_5	0.10	0.10	0.12	0.09	0.09	0.14	0.07	0.09	0.07	0.06	0.06	0.06
LOI	2.07	1.15	1.86	0.93	1.61	0.93	0.99	1.27	0.93	1.56	1.44	1.70
Total	100.1	100.3	100.4	99.9	100.0	100.0	100.2	99.6	99.6	99.6	99.5	100.0
Mg#	0.47	0.48	0.47	0.49	0.46	0.44	0.44	0.57	0.60	0.60	0.58	0.61
ASI	1.09	1.05	1.13	1.00	1.05	1.08	1.07	0.68	0.63	0.70	0.75	0.75
Trace elements (ppm)												
Li	39.4	36.0	49.9	34.2	60.3	89.1	66.2	27.3	25.4	23.9	44.2	38.7
Be	1.5	1.4	1.7	0.8	1.9	1.2	1.6	1.1	1.0	1.2	1.4	1.1
Cr	116	116	155	100	173	158	145	304	440	371	337	336
Co	11.6	12.7	29.5	8.25	12.6	9.29	6.11	25.5	45.4	27.2	32.8	42.0

5

Table 1 (continued)

Sample	Ch4	10	Ch1	Pa7	Pa21	Sa2	CSa15	EK4	E25	CESa4	EPa1	E17
Lithology	GD	GD	GD	GD	GD	MZG	MZG	EHMg	EHMg	EHMg	EHMg	EHMg
Ni	11.5	15.2	19.4	9.91	16.6	11.3	7.83	66.8	70.6	79.0	88.8	41.0
Rb	81.6	83.9	89.8	58.1	116	137	118	47.0	52.7	55.0	60.6	60.2
Sr	134	129	167	90.2	152	107	95.2	131	156	157	144	166
Y	16.5	16.9	24.8	10.4	30.7	18.0	11.1	31.5	31.5	64.4	51.5	17.2
Zr	109	106	120	80.2	90.2	69.3	70.4	31.4	31.3	10.7	25.8	33.7
Nb	8.61	9.04	11.2	6.00	10.9	9.91	7.59	6.76	7.35	9.18	7.76	6.25
Cs	4.79	8.28	9.77	11.7	13.7	15.0	12.2	6.86	6.05	6.51	8.44	4.83
Ba	276	223	256	164	255	234	200	133	261	212	144	262
La	19.2	30.5	26.9	12.8	29.1	26.3	23.0	23.1	20.9	24.7	20.2	16.2
Ce	40.0	57.1	52.7	26.9	55.2	50.0	46.6	54.8	47.8	64.7	54.4	34.4
Pr	4.93	7.13	6.88	3.21	7.33	6.30	5.50	8.22	7.28	11.4	9.35	4.36
Nd	17.6	21.7	22.8	10.3	23.9	19.6	19.4	28.2	25.8	44.1	36.6	14.3
Sm	3.41	3.98	4.89	2.16	5.23	3.98	3.50	6.42	6.31	12.3	10.2	3.02
Eu	0.70	0.80	1.04	0.45	0.92	0.67	0.52	0.92	1.06	1.02	0.98	0.89
Gd	3.23	3.69	4.74	2.14	5.34	3.74	2.97	6.12	6.24	13.0	10.1	2.96
Tb	0.56	0.67	0.93	0.42	1.12	0.75	0.45	1.23	1.30	2.77	2.14	0.56
Dy	3.45	3.28	4.63	2.16	5.78	3.58	2.47	6.55	6.48	14.2	10.9	3.04
Ho	0.70	0.76	1.14	0.51	1.42	0.83	0.47	1.53	1.57	3.38	2.57	0.75
Er	1.96	1.94	2.85	1.32	3.60	1.97	1.23	3.87	3.82	7.99	6.20	1.98
Tm	0.29	0.31	0.48	0.20	0.60	0.32	0.18	0.62	0.62	1.26	0.99	0.32
Yb	1.81	1.69	2.58	1.18	3.58	1.78	1.15	3.47	3.30	6.27	5.24	1.82
Lu	0.26	0.29	0.44	0.20	0.58	0.30	0.17	0.58	0.57	1.06	0.89	0.31
Hf	4.75	0.50	1.24	0.53	1.38	1.04	2.29	1.42	2.58	1.66	1.81	1.85
Ta	1.42	0.83	1.08	0.60	1.27	1.42	2.27	0.79	1.95	0.88	2.02	0.61
W	5.17	6.67	6.76	6.31	9.96	9.70	9.11	1.44	2.15	3.48	2.18	3.39
Pb	12.8	13.6	35.6	10.6	12.6	28.8	21.4	14.1	32.0	19.9	16.3	30.5
Th	11.5	11.6	11.7	7.52	16.2	15.6	18.9	5.02	3.26	9.02	3.67	5.74
U	2.45	1.93	2.06	2.20	2.59	2.00	2.41	1.22	0.87	2.02	2.14	1.40
Ce^N/Yb^N	5.82	8.88	5.36	5.98	4.05	7.38	10.6	4.15	3.81	2.71	2.72	4.96

Sample	ESalO	E19	E28	E29	E38	38	33	Asl5
Lithology	ELMg	ELMg	ELMg	ELMg	D	D	D	D
SiO_2	55.74	57.81	58.03	59.22	60.49	67.18	67.68	67.82
TiO_2	0.53	0.59	0.50	0.45	0.74	0.38	0.37	0.38
Al_2O_3	16.73	17.64	16.67	16.11	18.25	16.44	16.53	16.24
FeOt	7.83	7.00	7.87	8.12	5.04	2.93	2.82	2.76
MgO	5.17	4.05	4.55	4.64	2.32	1.58	1.58	1.55
MnO	0.19	0.15	0.18	0.21	0.93	0.03	0.02	0.02
CaO	7.03	5.66	6.99	5.86	4.67	3.00	2.76	3.15
Na_2O	3.02	2.60	2.01	2.35	4.38	3.97	4.01	4.03
K_2O	1.69	2.39	1.77	1.96	2.41	3.10	3.15	2.72
P_2O_5	0.08	0.09	0.07	0.07	0.17	0.10	0.10	0.10
LOI	1.67	1.78	0.97	0.46	0.78	1.03	1.13	1.43
Total	99.7	99.8	99.6	99.4	100.2	99.7	100.1	100.2
Mg#	0.54	0.51	0.51	0.50	0.45	0.49	0.50	0.50
ASI	0.85	1.03	0.93	0.97	1.00	1.07	1.10	1.06
Trace elements (ppm)								
Li	46.2	55.7	25.3	35.3	31.9	21.0	23.7	22.3
Be	1.4	1.2	0.8	1.4	1.3	1.3	1.3	1.5
Cr	175	96.5	104	165	35.4	60.6	88.9	90.1
Co	23.8	16.9	19.4	24.6	24.6	7.65	9.18	9.25
Ni	28.4	17.9	17.7	25.2	2.76	6.62	9.17	10.5
Rb	132	80.0	49.1	79.5	96.7	106	95.8	117
Sr	147	143	141	165	246	203	211	214
Y	28.1	17.4	11.6	14.7	15.3	7.20	8.50	10.1
Zr	22.3	82.2	35.7	37.3	142	148	149	169
Nb	9.32	8.37	5.83	7.16	15.6	10.6	11.6	12.5
Cs	11.7	18.3	5.17	6.22	18.1	14.8	24.0	12.4
Ba	219	186	173	225	298	275	292	306
La	32.2	18.4	12.7	15.4	19.0	11.8	12.1	13.3
Ce	60.2	35.9	24.3	29.8	34.8	20.2	22.0	22.7
Pr	7.58	4.50	2.94	3.70	4.17	2.24	2.53	2.61
Nd	22.7	14.9	9.77	12.2	13.8	6.91	8.07	8.09
Sm	4.57	3.19	1.91	2.67	2.88	1.40	1.70	1.64
Eu	0.74	0.80	0.85	0.95	1.06	0.54	0.55	0.65
Gd	4.48	3.20	2.02	2.51	2.83	1.42	1.69	1.69
Tb	0.94	0.63	0.40	0.51	0.56	0.26	0.31	0.34
Dy	4.95	3.27	2.12	2.62	2.81	1.45	1.69	1.80
Ho	1.22	0.83	0.56	0.65	0.70	0.32	0.42	0.43
Er	3.27	2.06	1.48	1.79	1.76	0.85	0.99	1.09
Tm	0.56	0.36	0.26	0.30	0.28	0.13	0.15	0.16

Table 1 (continued)

| Sample | ESalO | E19 | E28 | E29 | E38 | 38 | 33 | Asl5 |
Lithology	ELMg	ELMg	ELMg	ELMg	D	D	D	D
Yb	3.15	2.03	1.61	1.79	1.52	0.72	0.88	0.95
Lu	0.56	0.35	0.30	0.33	0.26	0.12	0.15	0.16
Hf	1.70	0.61	0.77	0.93	1.79	0.64	0.73	0.84
Ta	1.46	1.10	1.56	0.68	1.16	0.88	1.27	1.11
W	16.2	3.58	4.86	5.70	8.05	9.18	10.6	7.72
Pb	13.2	16.7	14.4	11.5	21.8	5.97	8.83	6.88
Th	20.3	10.3	2.92	2.05	7.63	8.21	8.75	11.2
U	4.65	1.94	0.71	0.70	1.30	1.35	1.74	1.92
Ce^N/Yb^N	5.02	4.64	3.96	4.37	6.01	7.35	6.57	6.29

FeO(t): total iron as FeO; (2) Mg#: mol MgO/MgO + FeO(t); (3) ASI: alumina saturation index = mol $Al_2O_3/Na_2O + K_2O + CaO$. QD: quartz-diorite; GD: granodiorite; MZG: monzogranite; EHMg: high-Mg enclaves; ELMg: low-Mg enclaves; D: dacite.

performed with a four-spectrometer JEOL JXA-8200 electron probe at university of Huelva (Spain), operated with an accelerating voltage of 15 kV and a probe current of 5 nA. Silicate standards were jadeite for Na, wollastonite for Ca, alkali feldspar for K and Al, enstatite for Mg, fayalite for Fe and Mn and apatite for P.

For determination of Sr and Nd isotopic ratios, whole-rock powdered samples were used. Rb–Sr and Sm–Nd isotopic ratios were determined with a Finnigan MAT-262 mass spectrometer at the University of Granada. Samples for Sr and Nd isotope analyses were digested using ultraclean reagents and analyzed by thermal ionization mass spectrometry (TIMS) in a Finnigan Mat 262 spectrometer after chromatographic separation with ion-exchange resins. Normalization values were $^{86}Sr/^{88}Sr = 0.1194$ and $^{146}Nd/^{144}Nd = 0.7219$. Blanks were 0.6 and 0.09 ng for Sr and Nd. The external precision (2 sigma), estimated by analyzing 10 replicates of the standard WS-E (Govindaraju et al., 1994), was better than ±0.003% for $^{87}Sr/^{86}Sr$ and ±0.0015% for $^{143}Nd/^{144}Nd$. $^{87}Sr/^{86}Rb$ and $^{143}Sm/^{144}Nd$ were directly determined by ICP-MS following the method developed by Montero and Bea (1998), with a precision better than ±1.2% and ±0.9% (2 sigma) respectively. Nd isotopic ratios were corrected for mass fractionation using a $^{146}Nd/^{144}Nd$ ratio of 0.7219. The results are reported in Table 2.

5. Petrography

5.1. Quartz diorites

These rocks have granular to porphyritic textures with plagioclase megacrysts. They are predominantly composed of plagioclase (40–50% vol.%), amphibole (5–10% vol.%), biotite (15–20% vol.%), alkali feldspar (<5% vol.%) and quartz (~10% vol.%). Plagioclase appears as anhedral to subhedral plates, zoned and altered to sericite, epidote and calcite. Biotite occurs as brown flakes, deformed and altered to chlorite, sphene, prehnite, muscovite, opaques, and quartz. Biotite is frequently associated with amphibole, which predate biotite in the crystallization sequence. Amphibole shows a euhedral prismatic habit, green colour, and it is often twinned, associated with biotite and altered to chlorite, epidote and prehnite. Quartz occurs as both anhedral to subhedral crystals and as a late interstitial phase. Alkali feldspar is anhedral to subhedral. Zircon, titanite, apatite are conspicuous accessory minerals. Minor alteration products are sericite, chlorite, epidote, prehnite, and calcite. Orthopyroxene (En_{56-58}) has been observed only in one sample. It is partially replaced to anthophyllite at the rims (Fig. 2a).

5.2. Granodiorites

They are coarse-grained, mesocratic rocks mainly composed of plagioclase (30–40 vol.%), quartz (25–30 vol.%), biotite (5–15 vol.%). amphibole (5–10% vol.%) and K-feldspar (<10 vol.%). Accessory minerals are apatite, zircon and allanite. Plagioclase is normally zoned, forming euhedral to suhedral crystals. K-feldspar is perthitic and appears as anhedral to subhedral crystals. Quartz forms anhedral crystals or aggregates of several grains with irregular boundaries. It occupies the interstices between feldspars and often displays undulatory and lamellar extinction indicative of incipient solid-state deformation. Amphibole shows a characteristic euhedral prismatic habit, green colour, and twinning. It is associated with biotite (Fig. 2b). Amphiboles show $Ca_B > 1.5$ (1.7–1.85), $(Na + K)_A < 0.5$ (0.12–0.25). They classify as calcic amphiboles according to Leake et al. (1997). In general, the composition may vary from magnesio-hornblende to actinolitic hornblende. Biotite is the most abundant mafic mineral in the studied samples. It is frequently associated with amphibole. Most biotite is altered to chlorite, or replaced by sphene, muscovite, opaques, and quartz. Biotite is highly aluminous (Al/Al + Si + Mg + Fe = 0.2–0.22) and ferrous (Fe/Fe + Mg = 0.49–0.53).

5.3. Monzogranites

These rocks have granular to porphyritic texture, with biotite-rich clots, feldspar megacrysts and quartz. Amphibole is present in some samples. Biotite crystals are variably transformed into chlorite and less commonly to epidote. Inclusions in alkali feldspar are apatite (Fig. 2c). Euhedral zircon and allanite are frequently associated with biotite. Plagioclase (An_{14-30}) is markedly zoned.

5.4. Dacites

Quartz, plagioclase and biotite occur as phenocrysts in a seriate texture (Fig. 2d). Normal alteration is to aggregates of chlorite, opaque minerals and epidote. These rocks contain numerous dark xenoliths, which show phenocrysts of pargasitic amphibole $[Ca_B > 1.5$ (1.71–1.77), $(Na + K)_A > 0.5$ (0.55–0.7); Fig. 2f] and plagioclase in a fine grain matrix of biotite and plagioclase.

5.5. Enclaves

Enclaves range in composition from diorite to monzodiorite. The crystal habit of K-feldspar together with zoned, euhedral plagioclase inclusions, suggest that they have an igneous origin (Vernon and Paterson, 2002). Their mineralogy and textures show that they have a typical multistage magmatic crystallization (Castro et al., 1991). Enclave minerals are essentially composed of plagioclase, amphibole and biotite (Fig 2e). Two types of enclaves are identified in Astaneh granitoids: (1) a fine- to medium-grained, weakly porphyritic, hornblende ± biotite gabbro and (2) fine-grained Qtz-diorites. These are the most abundant in the Astaneh

7

Table 2
Isotopic data from representative samples of the Astaneh intrusion.

Sample	Rock type	Rb (ppm)	Sr (ppm)	$^{87}Rb/^{86}Sr$	$^{87}Sr/^{86}Sr$	±2 sigma%	$(^{87}Sr/^{86}Sr)_i$	Sm (ppm)	Nd (ppm)	$^{147}Sm/^{144}Nd$	$^{143}Nd/^{144}Nd$	±2 sigma%	$(^{143}Nd/^{144}Nd)_i$	$\varepsilon_{Nd}(t)$	Tdm (Ma)
Sa11	Qtz-diorite	87.4	142	1.780	0.712726	0.003	0.70842	7.92	33.72	0.1414	0.512301	0.002	0.512143	−5.4	1.35
28	Qtz-diorite	86.3	140.9	1.772	0.712321	0.003	0.70804	3.49	15.6	0.1347	0.512256	0.0016	0.512110	−6.0	1.39
AS	Granodiorite	126	185.5	1.974	0.713007	0.001	0.70824	3.88	16.7	0.1406	0.512282	0.0006	0.512124	−5.8	1.37
AS16	Dacite	101	207.6	1.409	0.705449	0.003	0.70204	3.22	17.16	0.1130	0.512629	0.0019	0.512504	1.7	0.79

CHUR values: $^{87}Rb/^{86}Sr$ = 0.0847, $^{87}Sr/^{86}Sr$ = 0.7047, $^{147}Sm/^{144}Nd$ = 0.1967, $^{143}Nd/^{144}Nd$ = 0.51263. Errors in% relative at 2 sigma.
Initial ratios calculated at 170 Ma.

granitoids. Gabbroic enclaves range from 5 to 45 cm diameter (commonly 20–30 cm).

Amphibole, which may contain locally small relic inclusions of clinopyroxene, has a euhedral habit and classifies as magnesio-hornblende. It is associated with subordinate biotite. Plagioclase (An_{35-40}) is usually euhedral and zoned. Acicular apatite occurs as inclusions preferentially in plagioclase. Quartz (<10 vol.%) occupies the interstices between plagioclase crystals.

The fine-grained Qtz-dioritic enclaves are more abundant than gabbroic enclaves. They have porphyritic (plagioclase phenocrysts) and poikilitic textures. They are essentially composed of plagioclase (40–50 vol.%), amphibole (5–10 vol.%), biotite (15–20 vol.%), alkali feldspar (<5 vol.%) and quartz (<10 vol.%). The fine-grained matrix is composed of plagioclase laths an amphibole with interstitial quartz ± K-feldspar. Accessory minerals are iron oxides, apatite, zircon and titanite. They commonly show quenched textures such as acicular amphibole and acicular apatite, characteristic of rapid crystallization.

6. Geochemical features

6.1. Major elements

Representative whole rock major compositions of Astaneh granitoids and related rocks are reported in Table 1. Major element variations are illustrated in major oxide (harker) diagrams (Figs. 3 and 4). The rocks exhibit a range in SiO_2 from 52 to 71 wt.%. The abundances of Fe_2O_3, MgO, CaO, TiO_2, Al_2O_3 and MnO decrease with increasing SiO_2, whereas K_2O increases and Na_2O remains nearly constant. The enclaves show higher MgO, Fe_2O_3, TiO_2, CaO and lower K_2O, Na_2O and SiO_2 values than the granite samples. Granodiorites and Qtz-diorites, the most abundant rocks of the Astaneh intrusion, are well grouped in terms of major elements showing a regular variation with silica. This is characteristic of magmatic processes by either fractionation or partial melting. The relations with the other magmatic groups are more complex. Enclaves are plotted along the same linear trend than granodiorites and Qtz-diorites, coincident in general terms with the typical trend of calc-alkaline batholiths and continental margin andesites (Figs. 3 and 4). This is so for CaO, FeO and MgO. However, enclaves depart from the general calc-alkaline array for other elements as Al_2O_3, TiO_2 and alkalis. The most outstanding distinction is an increase of alumina with silica. These enclaves have an average andesite composition for diagnostic elements such SiO_2, MgO and CaO. However, they are depleted in TiO_2, Na_2O and Al_2O_3 with respect to the andesite trend (e.g. the Cascades trend shown in the diagrams). Most granodiorites and associated mozogranites and Qtz-diorites are metaluminous to slightly peraluminous, with Al saturation index (ASI = mol $Al_2O_3/Na_2O + K_2O + CaO$) within the range 1.0–1.09 in the more mafic Qtz-diorite group and 0.97–1.13 in the granodiorite-monzogranite group. Also some enclaves are slightly peraluminous with ASI from 0.68 to 1.03 (Table 1).

A relevant feature is the silica gap observed between the two groups, enclaves and host granodiorites and Qtz-diorites. The silica gap (59–62 wt.% SiO_2) is in agreement with the sharp boundary between enclaves and host granordiorites and the absence of any transitional or intermediate rock. A second silica gap is observed between monzogranites and granodiorites (66–69 wt.% SiO_2). However, in this case the origin of the gap may be due to the scarcity of samples (two analyzed samples) from the mosnzogranite group.

Interesting variations are also observed between major oxides and molar ratios. These are shown in selected diagrams in Fig. 4. The CaO–MgO diagram is diagnostic for magmatic series related by fractionation or melting trends. All the samples from Astaneh
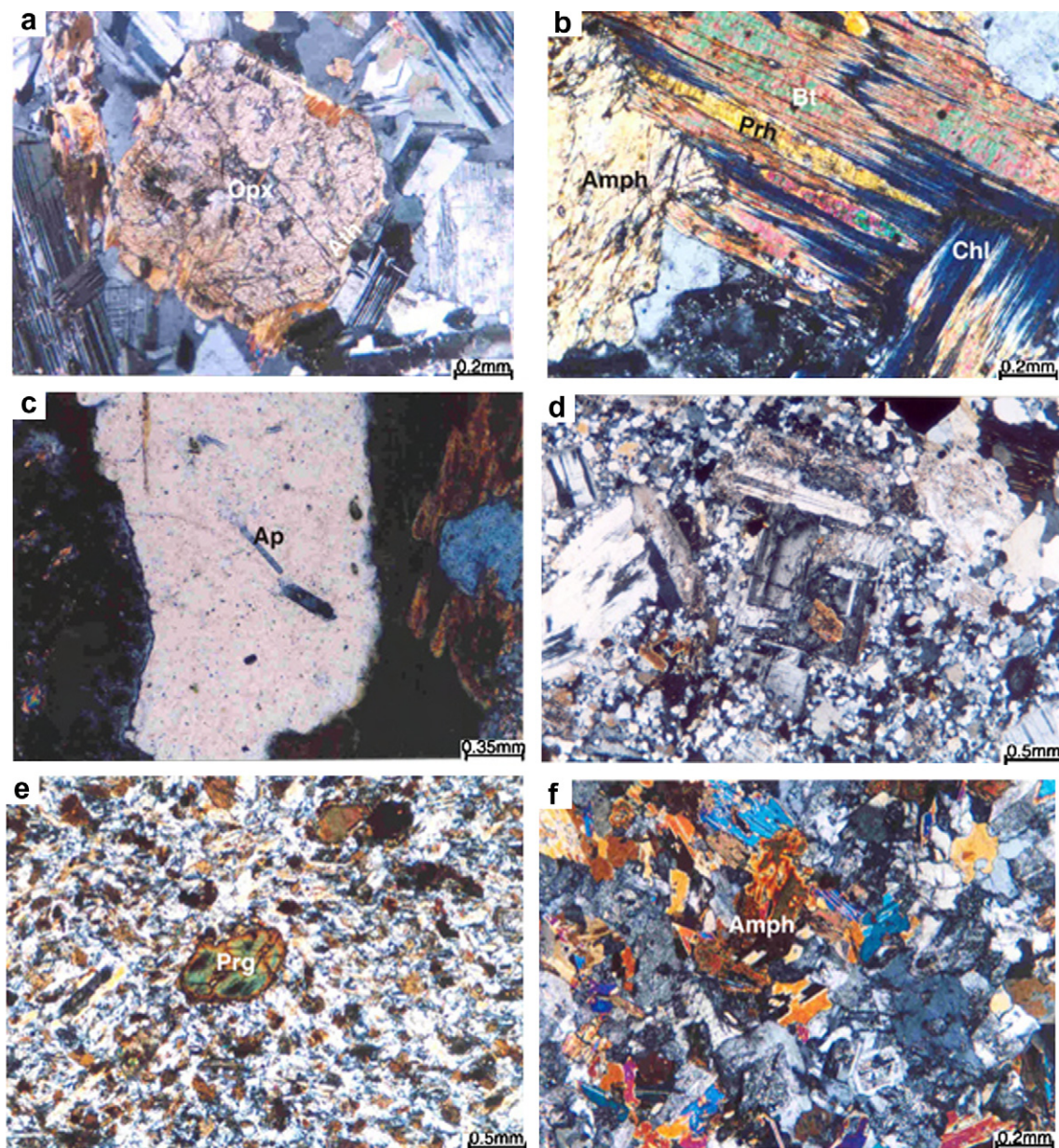
Fig. 2. Microphotographs of representative samples (crossed polarized light) from the Astaneh intrusion. (a) Orthopyroxene in quartz-diorite. (b) Biotite replaced by chlorite and prehnite. (c) Needles apatite in K-feldspar. (d) Porphyritic texture in the rhyodacite. (e) Microgranular enclaves. (f) Amphibole (Pargasite) in an enclave of the rhyodacite. Mineral abbreviations are according to Kretz (1983).

follow a regular curved trend very close to the trend displayed by andesites and calc-alkaline batholiths (Fig. 4a). However, the gaps mentioned above for SiO_2 are also present in this diagram. A similar curved trend is observed in the diagram plotting K# (mol K_2O/ $K_2O + CaO$) against wt.% MgO (Fig. 4d). Two groups of enclaves are distinguished in these diagrams according to the MgO content. A more primitive group with MgO > 6.0 wt.% (high-Mg enclaves) and a more evolved group with MgO < 6.0 wt.% (low-Mg enclaves). This distinction is not so clear in the silica variation diagrams. These two groups will be analyzed in terms of trace elements in the next item. Series classification diagrams are shown in Fig. 4c, d. All the Astaneh rocks plot in the subalkaline field of the TAS diagram (Fig. 4c). They define a regular trend almost coincident with the trend of calc-alkaline andesites and batholiths from the North America active continental margin (Cascades andesites and plutonic rocks from the Sierra Nevada and Peninsular Ranges batholiths). In the K_2O-silica diagram (Fig. 4d) the Astaneh rocks

follow a linear trend evolving from normal calc-alkaline to high-K calc-alkaline fields. In general terms, the Astaneh rocks are rich in K and they plot close to the upper limit of the typical calc-alkaline trends. Enclaves plot in these diagrams very close to the more mafic members, namely basaltic andesites and high-Mg primitive andesites of the Shasta volcanics from the cascades. These comparisons will be used for petrogenetic considerations of the Astaneh intrusion.

6.2. Trace elements

Trace element abundances were determined for representative samples of the Astaneh intrusive complex (Table 1). Fig. 5 shows primordial mantle (Sun and Mc Donough, 1989) normalized diagrams for the six groups of rocks distinguished in the Astaneh intrusion. The group of Qtz-diorites is taken for comparison with other groups. Also included for comparison is the pattern of aver-
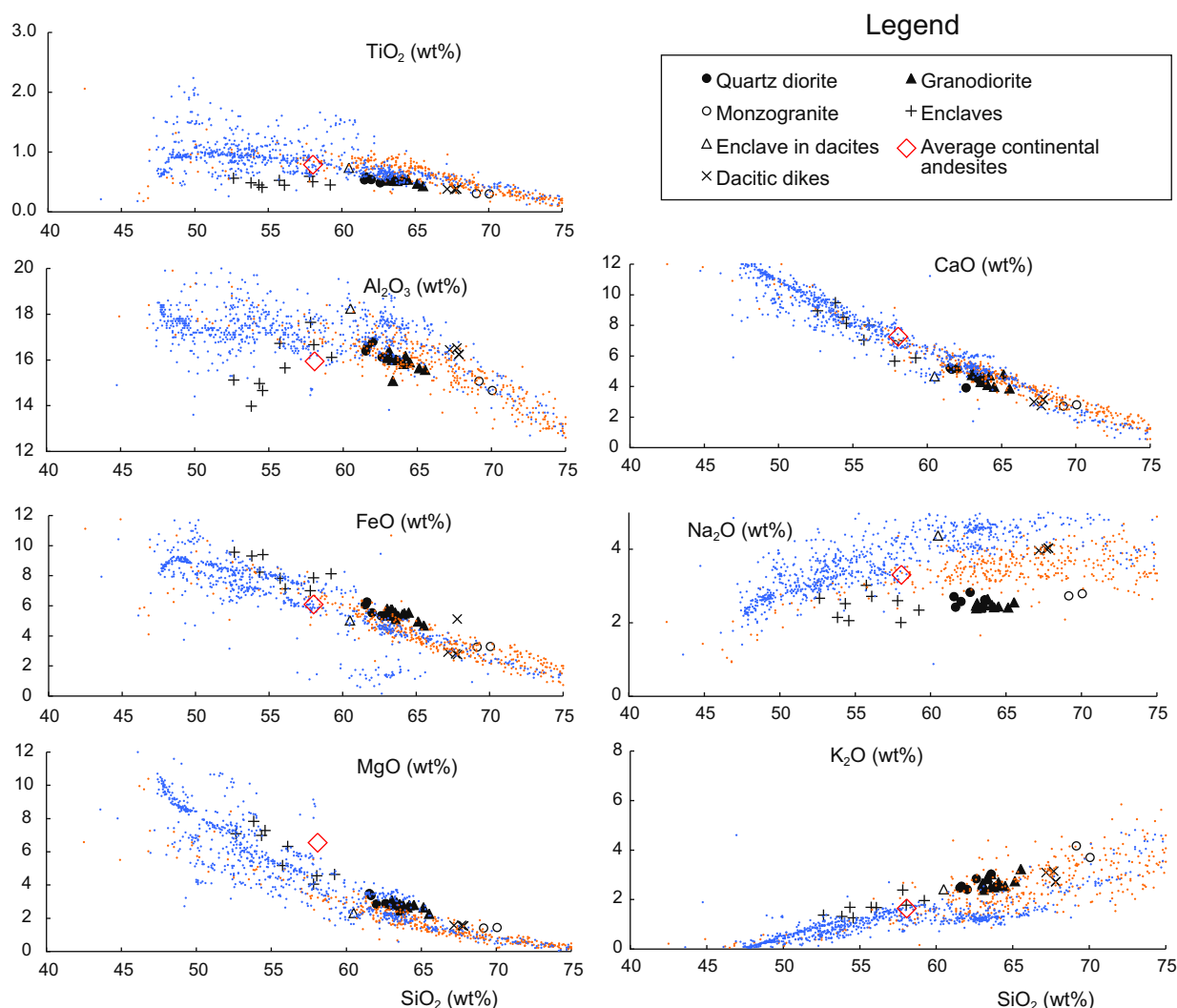
Fig. 3. Silica variation diagrams of igneous rocks from the Astaneh intrusion. Data from calc-alkaline rocks from the N America margin are shown for comparison: Sierra Nevada and Peninsular ranges batholith (red dots; data from Lee et al. (2007)) and Cascades andesites from Medicine Lake, Mt. Shasta, Mt. St. Helens and Mt. Larsen (data from GEOROC data base in http://georoc.mpchmainz.gwdg.de/georoc/). (For interpretation of the references to colour in this figure legend, the reader is referred to the web version of this article.)

age continental andesites taken from Kelemen et al. (2003). Granodiorites and Qtz-diorites have very similar patterns.

These similarities confirm the major-element affinities between these two groups. Compared to average andesites, all rocks from Astaneh share depletion in Ba, Sr and P. Moreover, they show the typical Pb enrichment and Ti depletion that characterize crustal signatures in arc magmas. Enclaves show a marked enrichment in HREE compared to the other groups and also compared to the average continental andesites. With exception of the Ba, Sr, P depletion, the rocks of Astaneh share the most relevant features of arc magmas. The available data are not enough for identification of regional anomalies. An assessment of these geochemical anomalies will require further geochemical studies in other intrusive massifs associated to the same magmatic system.

Similar comparisons can be made in terms of REE (Fig. 6). In general, the Astaneh rocks exhibit strongly fractionated REE patterns (La/Yb = 2.57–22.04) with variable Eu anomalies (Eu/Eu* = 0.24–1.33). Granodiorites are enriched in HREE compared to Qtz-diorites. However, these two groups and the monzogranites show strong similarities suggesting that they form part of a single magma series. However, enclaves display markedly distinct patterns compared to the diorite-granodiorite series. The two groups of enclaves that were identified by petrography mineral assem-

blages can be distinguished in terms of the REE patterns. The gabbroic group is strongly enriched in HREE with a large Eu anomaly. The Qtz-diorite group is formed by less depleted compositions showing little or null Eu anomaly. Some samples of this second group are similar to the Qtz-diorites. Interestingly, these two groups correspond to the high-Mg and low-Mg enclaves respectively (Fig. 7), suggesting that they form two separate groups with different origins though they are collinear in major element variation diagrams. High-Mg enclaves are also richer in Ni compared to low-Mg group (Fig. 7a), supporting the separation in two groups with possible differences in magma generation and source compositions.

Primordial mantle normalized diagrams (Fig. 5) also show marked affinities between Qtz-diorites and granodiorites. However, the Astaneh Qtz-diorites show a marked depletion in Ba and Sr departing from the typical trend of continental andesites. Again, the available data are not enough to establish regional or local anomalies. Granodiorites and monzogranites display similar patterns (Fig. 5b and c) compared to Qtz-diorites. Enclaves are markedly different (Fig. 5d) form the former groups. However, they share with the Qtz-diorite-granodiorite group a marked depletion in Ba. Dacites (Fig. 5e and f) show patterns almost identical to granodiorites as they are the volcanic-subvolcanic equivalents.
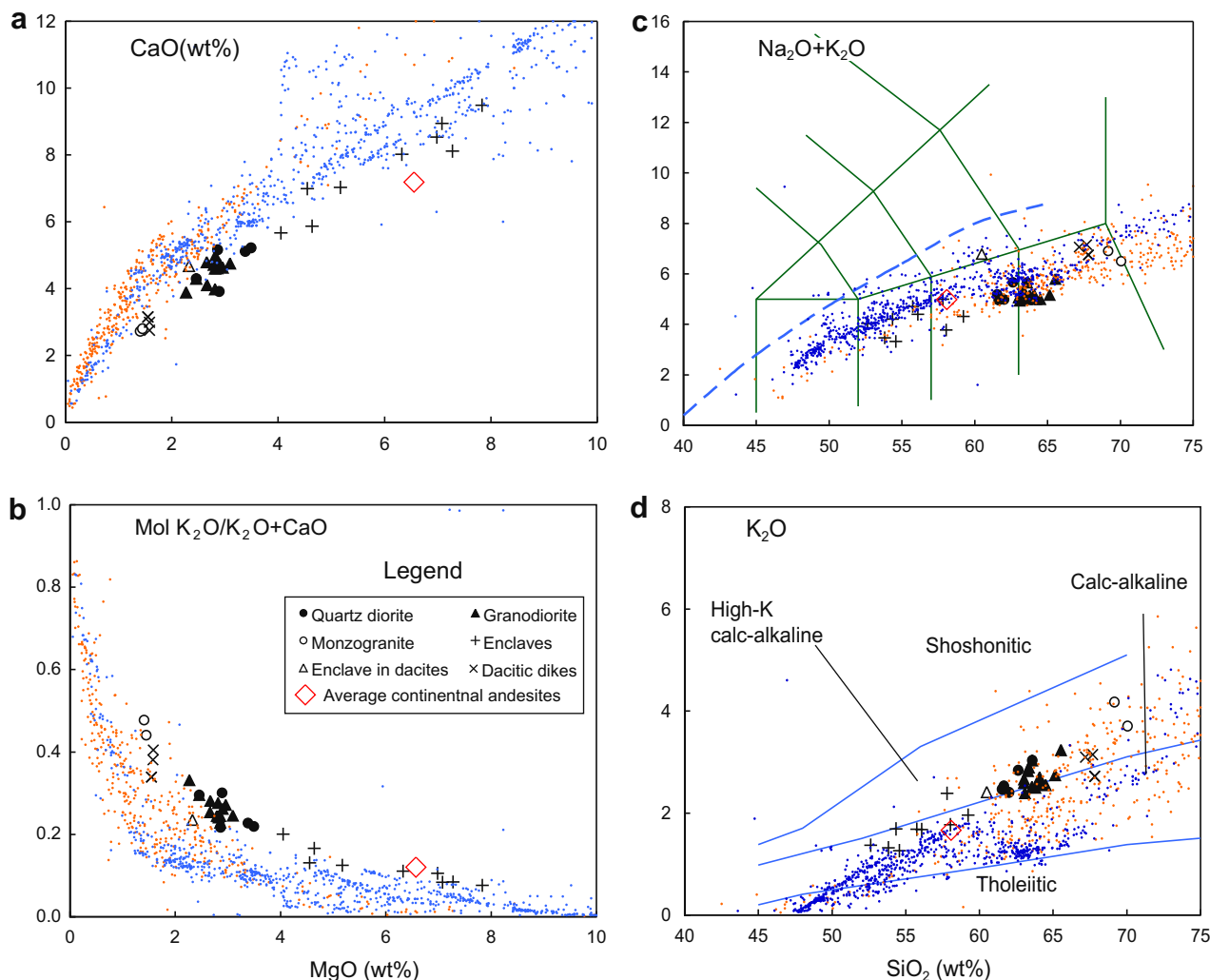
Fig. 4. Major oxide plots showing the general magmatic trend of the Astaneh intrusive rocks compared with the typical calc-alkaline trends of batholiths and andesites.

6.3. Isotopes

Isotopic ratios for $^{143}Nd/^{144}Nd$ and $^{87}Sr/^{86}Sr$ of the Astaneh granitoids and subvolcanic rocks are listed in Table 2. The initial $(^{87}Sr/^{86}Sr)_i$ ratios and $\varepsilon_{Nd}(t)$ values have been calculated at 170 Ma on the basis of zircon U–Pb datings (Ahmadi Khalaji, 2006). The data are shown in a plot of $\varepsilon_{Nd}(t)$ vs. $(^{87}Sr/^{86}Sr)_i$ in Fig. 8. All the granitoids plot in the lower right quadrangle, corresponding to crustal signatures. With exception of the dacite sample, granodiorites and Qtz-diorites are grouped within a narrow interval. These relations are consistent with the geochemical affinity of these two groups in terms of major and trace elements. Low negative ε_{Nd} values in the Astaneh rocks may suggest an important implication of old crustal materials in their genesis. These inferences are analyzed in detail below. However, the scarcity of isotopic data in this study, and also in other adjacent plutonic areas within the SSMZ, precludes the elaboration of a definitive petrogenetic model, which is pending for further studies.

7. Discussion

7.1. Origin of the parental magmas

A relevant feature of the Astaneh intrusion is the close relation found between Qtz-diorites and granodiorites. Both form part of a magma series in a very similar way to the calc-alkaline series in active margins. In this sense, the comparisons made with the typical cordilleran batholiths and the Cascades andesite suits of the North America pacific margin are very useful to address petrogenetic estimations. Another relevant feature of Astaneh is the presence of two well-distinguishable groups of magmatic enclaves. One of them, the low-Mg group, has clear affinity with the Qtz-diorites. The other group of enclaves, the high-Mg group, is characterized by a more primitive chemistry, with Mg# values (Mg# = molar $MgO/MgO + FeO$) around to 0.6 and high Ni contents (>50 ppm), both indicative of equilibrium with the peridotite mantle. At the same time, this Mg-rich group is enriched in HREE and other HFS incompatible elements. Both the primitive character (high Mg#, high Ni content) and the high content in incompatible elements are characteristic features of magmas derived by melting of an enriched mantle source in a suprasubduction environment (Tatsumi et al., 2003; Martin et al., 2005). However, a petrogenetic link relating these primitive magmas and the other intermediate and felsic rocks, namely Qtz-diorites and granodiorites, of the Astaneh intrusion cannot be established in the light of the available data. The petrogenetic link by means of either fractional crystallization or partial melting is discussed later.

Most of the samples of the Astaneh pluton belong to the I-type granites of Chappell and White (1974). Regarding the origin of these calc-alkaline felsic and intermediate magmas, two groups of hypotheses have been proposed. According to the first group,
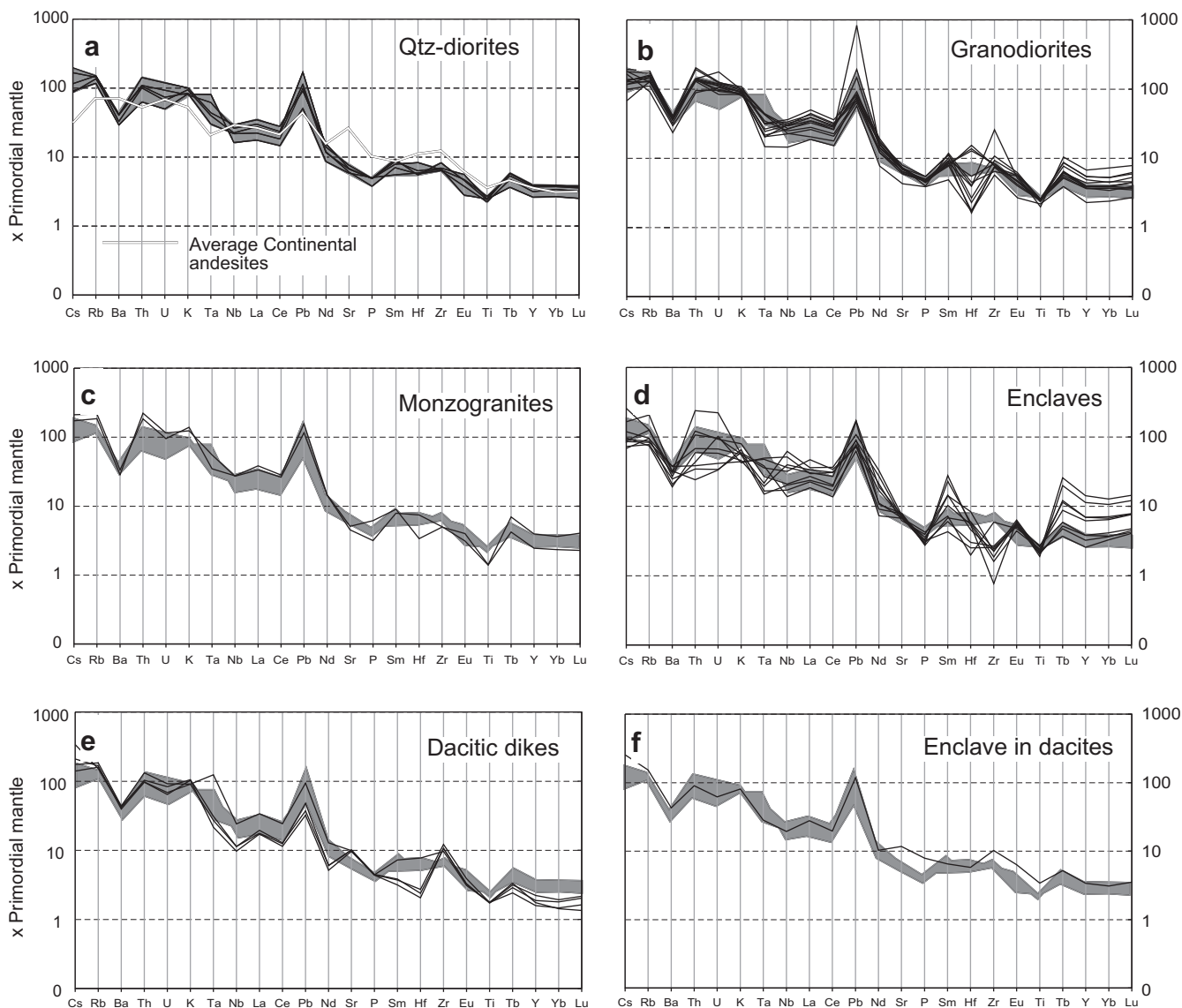
Fig. 5. Primitive mantle-normalized spider diagrams (Sun and Mc Donough, 1989). The slight enrichment in Ta may be caused by contamination with CW mortars during crushing. See text for further explanations.

felsic arc magmas are derived from basaltic parent magmas by assimilation, fractional crystallization (AFC processes; De Paolo, 1981). In the second group of hypotheses, basaltic magmas provide heat for the partial melting of crustal rocks (Annen and Sparks, 2002; Huppert and Sparks, 1988). Combined models including heat and fluid transfer to the continental crust by wet-basalt magmas have been also proposed (Annen et al., 2006; Thompson et al., 2002). The low concentration of MgO, low content in transition elements (Ni, Cr, Co, V), the large volume of the granitoid rocks and the absence of rocks with basaltic compositions (all samples have SiO_2 content >52%, Table 1) in the Astaneh area, suggest that fractionation from a basaltic parent magma is unlikely.

Large-scale melting of a mafic crustal source may have been favored by high heat flow during Cimerian Orogenesis by underplating of mantle-derived magmas into the crust. Consequently, it can be argued that the Astaneh rocks originated by partial melting of crustal protoliths in an active margin. Basaltic magma may contribute to the thermal budget; so, the calc-alkaline granitoids seem to reflect, essentially, hydrous partial melting of mafic lower crust (and/or basic under plate) rather than direct origin from a man-

tle-derived parent magma. Some experimental data supports that hydrous melting of basalt can produce tonalitic–trondhjemitic magmas (e.g. Wyllie, 1984) that might evolve by fractionation and/or crustal contamination toward more granitic compositions. The second part of the process is needed to account for the enrichment in K and incompatible elements. However, little evidence is supplied about a relevant role of crustal assimilation to produce the observed geochemical trends. Independently of a more or less effective crustal assimilation, it is a fact that the more primitive magmas, the high-Mg group of enclaves, in Astaneh are the most enriched in incompatible elements, pointing to an enriched mantle source. Furthermore, it is very unlikely that high-K granites can be produced directly by melting of low-K basalt and metamorphic equivalent (amphibolite), without involvement of a K rich sedimentary component (Winther and Newton, 1991). The Sr–Nd isotopic ratios also point to an important participation of a crustal source in the generation of the magmas.

Experimental melts derived from partial melting of different crustal source rocks such as felsic pelites, metagreywackes, gneisses and amphibolites fall into distinct fields based on the major
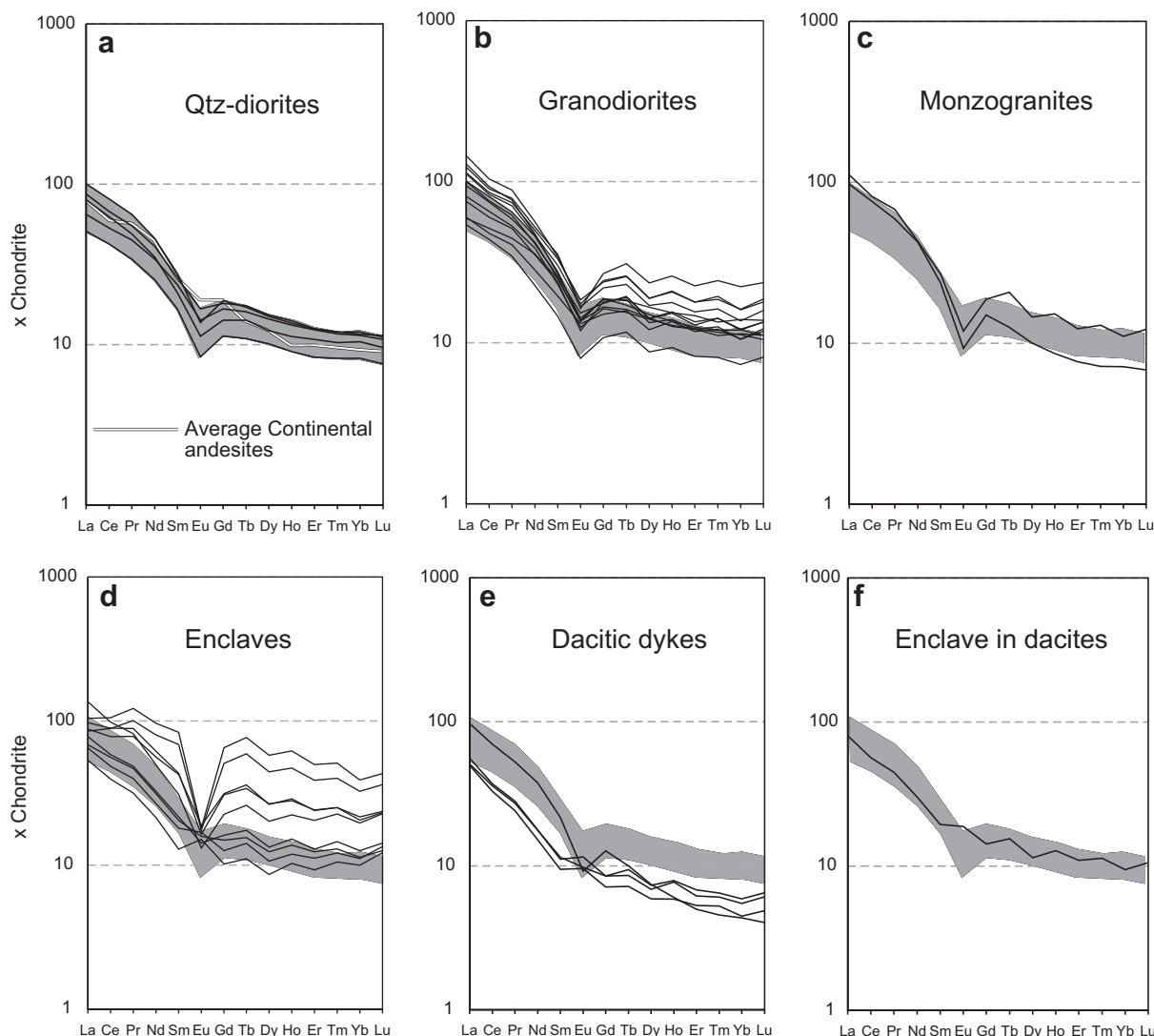
Fig. 6. Chondrite-normalized (Nakamura, 1974) REE patterns of representative samples of the Astaneh intrusion. See text for explanations.

oxide ratios or molar ratios (Patiño Douce, 1999). The Astaneh rocks are characterized by low ratios for $Al_2O_3/FeO + MgO + TiO_2$ (1.1–3.46), $Na_2O + K_2O/FeO + MgO + TiO_2$ (0.37–1.4) and $Al_2O_3/MgO + FeOt$ (0.42–2) and a rather high range of $CaO/(FeO + MgO + TiO_2$ (0.44–0.67). These values support that these magmas cannot be originated by partial melting of pelites (Fig. 9). Most of the Astaneh rocks (and the adjacent Boroujerd rocks used here for comparisons) generally plot in the amphibolite and metabasalt-metatonalite fields (Fig. 9a and d). This feature, associated with relatively high Mg# values (0.35–0.61) precludes a derivation from felsic pelite and/or metagreywacke. Thus, the possible implication of a mafic source (diorite?) with addition of some recycled material (sediments?) in the source region is considered here.

7.2. Derivation of granodiorites (and monzogranites) by partial melting and/or equilibrium fractionation of a diorite precursor

The possibility that granodiorites were derived by partial melting of a diorite source or fractional crystallization of a wet diorite magma was analyzed in detail by Sisson et al. (2005) means of laboratory experiments and applied to the some cordilleran granites of the Sierra Nevada batholith (Ratajeski et al., 2005). The strong similarity between the plutonic associations described by these authors and those described here in the Astaneh complex, suggests that the application of this hypothesis must be taken into account in this study. Diorite inclusions in Astaneh may represent the source material, either the parental melts or solid source, from which the granodiorite magmas were possibly extracted by either fractionation or partial melting. It can be remarked the close similarity between these diorites (e.g. sample CESa4, Table 1) and the Hb-diorite used by Sisson et al. (2005) in their experiments (YOS-55A, Sisson et al., 2005, their Table 1). For this reason, we have used this sample to model melt and magma composition by means of the MELTS algorithm (Ghiorso and Sack, 1995). A proxy for melting of a similar source is given by the experiments by Patiño Douce (1995) and Castro et al. (1999) by using a composite source (basalt + pelite) of a broad andesite composition. The results of these experiments produced abundant melt (30–60 vol.%) of granodiorite composition leaving a noritic residue at conditions of medium and lower crust and at temperatures of 900 and 1000 °C. The application of the MELTS algorithm produced interesting results that will be summarized here.

Table 3 shows the composition of a melt extracted at 30% of partial melting (or 30% remaining liquid in equilibrium crystallization) at 875 °C (QFM buffer) and 8 kbar from diorite CESa4. The value of 30% is justified because this is the lower rheological
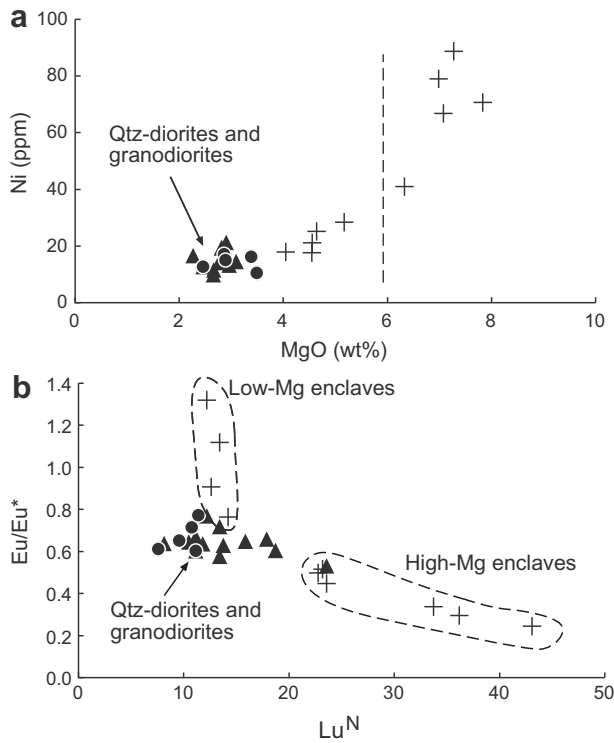
Fig. 7. Diagrams showing the distinction between the two groups of microgranular enclaves of Astaneh. The high-Mg group (MgO > 6 wt.%) is the richer in Ni (a). The two groups are also distinguished by the REE contents and Eu/Eu* values (b).

rich restites from the source. The two possibilities are analyzed here.

Increasing temperature and, hence, the melt fractions, has the limit imposed by the minimum silica content in the resulting melt. Melts developed at high melt fractions may contain large amount of Fe and Mg dissolved in the melt but, at the same time, they may have silica contents below the minimum required for granodiorites (63 wt.% SiO_2). This limit is found at 1024 °C and 8 kbar for the studied sample (Table B). The amount of melt produced at these conditions is about 50 wt.%. However, if this melt is compared with a typical granodiorite from Astaneh (sample Csa25) it is still poorer by half in Fe and Mg (Table 4).

Thus, the way of increasing melt fraction to get the granodiorites by either partial melting or equilibrium crystallization is very unlikely. A different source, necessarily more felsic, is required. Another possibility is that granodiorites are not pure melts but represent magmas with a high crystal content (restites and/or cumulates) dragged from the source. This is also analyzed here below.

The composition of the residue left at 30.2 wt.% melt fraction, calculated by means of the MELTS algorithm, is shown in Table 3. The average composition of this residue may be mixed in variable proportions producing magmas with variable contents in Fe and Mg. Table 5 shows the results of mixing variable amounts of solids, formed in equilibrium at the source region, with melts produced at 30 wt.% melt fraction (Table 3). There is a close similarity between the mixture with 30 wt.% restite and the granodiorite CSa25. Thus, variable separation of entrapped crystals from the source seems to be an efficient mechanism in accounting for the observed chemical composition of granodiorites. This mechanism is more favorable than increasing the melt fraction, as demonstrated here by using the results of the MELTS algorithm. However, it is unclear if granite melts may carry and transport for many km a so high content of solid material from the source. Amphibole polycrystalline clots are identified as restites derived from a pyroxene precursor in calc-alkaline granodiorites (Castro and Stephens, 1992; Stephens, 2001). However, these mafic restites represent a small fraction of the whole mafic components in granodiorites, the rest showing textural evidence of crystallizing from the magmas. Consequently, Absence of any evidence for so high restite content is a handicap in

threshold (Didier and Barbarin, 1991) that allows the melt to be extracted from the source. However, the composition of melt generated at this melt fraction is far from the average granodiorite composition. The granodiorite CSa25 from Astaneh may be taken for comparison. This is much higher in Fe and Mg compared with the theoretical melts. There are two ways to increase the Fe and Mg content in the melt: (1) by increasing the temperature and melt fractions, and (2) by mixing the extracted melt with Fe- and Mg-
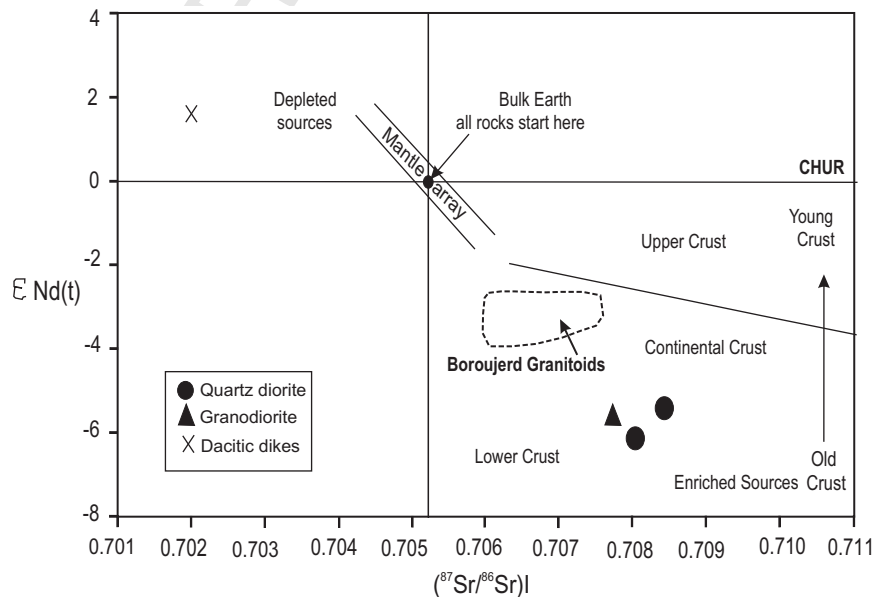

Fig. 8. Initial $\varepsilon_{Nd}(t)$ values vs. initial Sr isotopic ratios of analyzed samples from the Astaneh intrusion. The field of isotopic data in the Boroujerd area (Ahmadi-Khalaji et al., 2007) is shown for comparison.
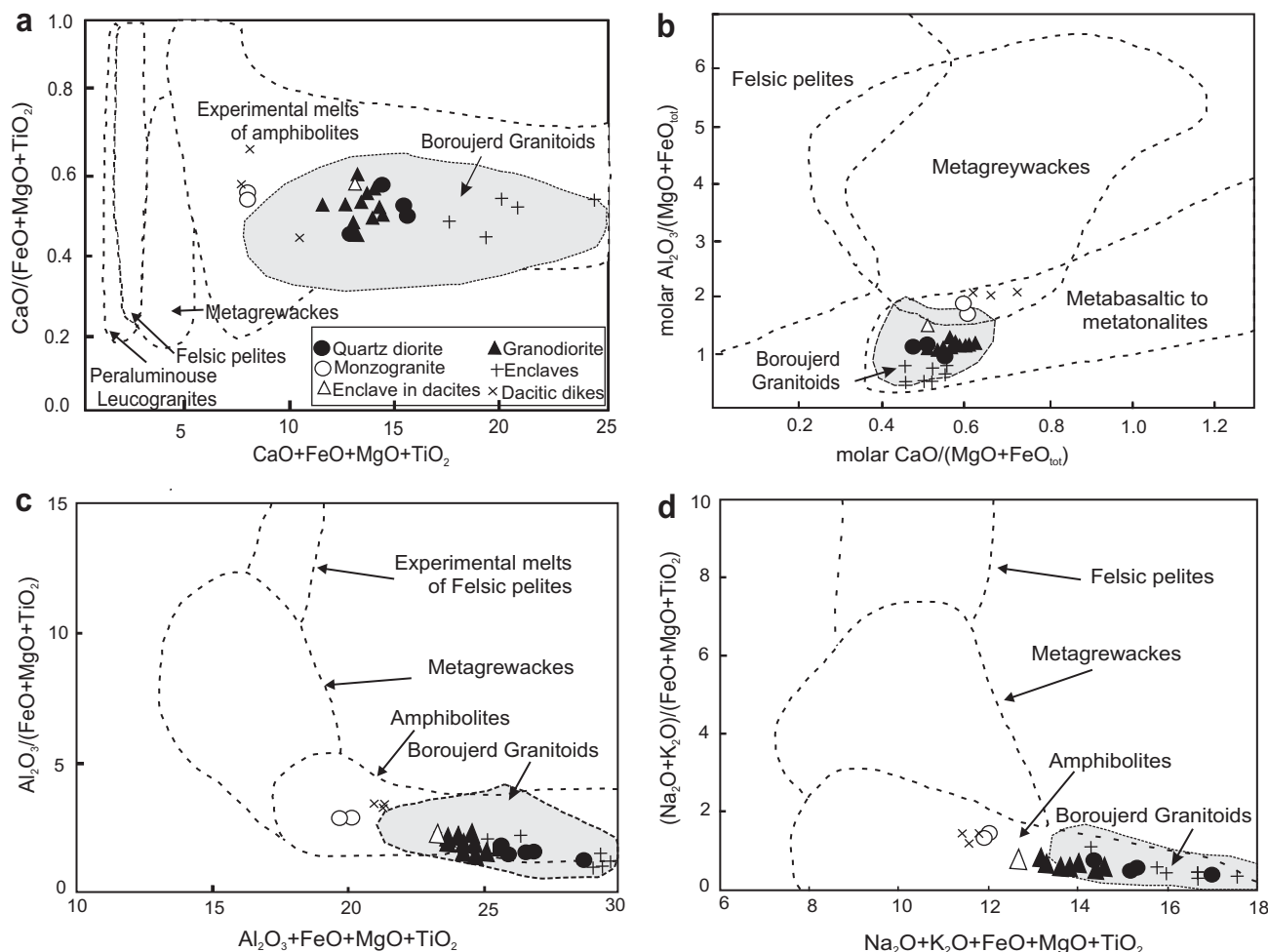
Fig. 9. Astaneh granitoids plotted on the (a) CaO/FeO + MgO + TiO$_2$ vs. CaO + FeO + MgO + TiO$_2$ (b) Al$_2$O$_3$/MgO + FeOt vs. CaO/(MgO + FeOt); (c) Al$_2$O$_3$/(FeO + MgO + TiO$_2$) vs. Al$_2$O$_3$ + FeO + MgO + TiO$_2$ and (d) Na$_2$O + K$_2$O)/FeO + MgO + TiO$_2$ vs. Na$_2$O + K$_2$O + FeO + MgO + TiO$_2$ (Patiño Douce, 1999 and references therein). Shaded areas show the field of Boroujerd granitoids (Ahmadi-Khalaji et al., 2007).

accepting this genetic mechanism from a diorite or gabbroic source.

It seems that the Astaneh diorite inclusions unlikely represent the source from which the granodiorites were generated. A more silicic source must be involved to generate these granodiorite melts. Alternatively, the source may be represented by a subducted mélange that undergone partial melting within the mantle at the core of a cold diapir (cold plumes). The composition of these mélanges can be very close to andesites. Thus, the experiments with composite sources (Patiño Douce, 1995; Castro et al., 1999;

Table 3
MELTS calculations of phase compositions at 30% melting of the CESa4 Qtz-diorite of Astaneh intrusion.

	Melt	Cpx	Grt	Opx	Pl
wt.% phases	30.21	28.8	21.31	3.64	15.13
SiO$_2$	66.16	50.88	39.63	52.78	61.73
TiO$_2$	0.29	0.74			
Al$_2$O$_3$	15.99	5.44	22.41	2.38	23.7
Fe$_2$O$_3$	0.18	1.17		0.36	
FeO	0.67	7.3	21.96	20.12	
MnO	0.77				
MgO	0.36	13.12	9.82	23.11	
CaO	1.92	20.32	6.18	1.16	5.15
Na$_2$O	3.71	1.03			7.34
K$_2$O	4.58				2.09
P$_2$O$_5$	0.2				
H$_2$O	5.19				
Total	100	100	100	100	100

Table 4
MELTS calculations of liquid compositions with increasing T from CESa4 Qtz-diorite of Astaneh intrusion.

Pressure	8 kbar	8 kbar	8 kbar	8 kbar	8 kbar	Granodiorite
Temperature	760	875	960	1025	1090	CSa25 Astaneh
Wt.% melt	20	30	40	50	60	
SiO$_2$	75.67	69.78	66.34	63.3	59.66	63.59
TiO$_2$	0.11	0.3	0.5	0.52	0.54	0.52
Al$_2$O$_3$	13.73	16.86	18.61	20.09	21.19	16
Fe$_2$O$_3$	0.08	0.19	0.37	0.56	0.8	
FeO	0.25	0.71	1.53	2.61	4.13	5.06
MnO	1.23	0.81	0.61	0.48	0.4	0.1
MgO	0.22	0.37	0.6	0.91	1.51	2.46
CaO	1.65	2.02	2.68	3.47	4.73	4.3
Na$_2$O	3.31	3.91	4.4	4.47	4.02	2.63
K$_2$O	3.42	4.83	4.21	3.48	2.92	3.03
P$_2$O$_5$	0.32	0.21	0.16	0.12	0.1	0.11
H$_2$O	0.00[a]	0.00[a]	0.00[a]	0.00[a]	0.00[a]	1.54
Total	100	100	100	100	100	99.34

Same conditions than Table 3.
[a] Melts recasted to an anhydrous base.

Table 5
Composition of liquid plus restite mixtures from MELTS calculations with CESa4 Qtz-diorite of Astaneh intrusion.

% of restite	10	20	30	Gd CSa25
SiO$_2$	67.7	65.63	63.59	63.59
TiO$_2$	0.3	0.3	0.3	0.52
Al$_2$O$_3$	16.62	16.38	16.14	16
Fe$_2$O$_3$	0.23	0.26	0.29	
FeO	1.78	2.84	3.89	5.06
MnO	0.72	0.64	0.56	0.1
MgO	1.36	2.33	3.29	2.46
CaO	3.03	4.02	5	4.3
Na$_2$O	3.72	3.52	3.33	2.63
K$_2$O	4.37	3.91	3.47	3.03
P$_2$O$_5$	0.19	0.17	0.14	0.11
H$_2$O	0[a]	0[a]	0[a]	1.54
Total	100	100	100	99.34

Same conditions than Table 3.
  [a] Melts recasted to an anhydrous base.

Castro and Gerya, 2008) are equally applicable to the generation of granodiorites by partial melting and partial restite unmixing.

The origin of an andesite precursor, either as a subducted mélange or underplated andesite magmas, is out of the scope of this study. However, a simple generation from a mantle source is not so straightforward. Part of the Astaneh inclusions represented by the high-Mg enclaves show evidence of derivation from a metasomatised mantle source (high Mg#, high Ni contents). However, we have shown that derivation of a silicic melt of granodiorite composition from this source, either as solid or parental magma, is very unlikely. We propose that the parental magmas for granodiorites and monzogranites of Astaneh are possibly the Qtz-diorites. They have silica contents, as well as the other major elements, very close to the composition of subducted mélanges. Also we have shown in this paper that Qtz-diorites and granodiorites form a magmatic trend that can be interpreted as either a magma fractionation trend or incremental melting from a solid source with the composition of a Qtz-diorite. Consequently, the melting, total or partial, of a composite source of the kind of a subducted mélange (=Qtz-diorite, =andesite) composed by sediments and oceanic crust, may account for the observed magma compositions satisfactorily (Castro and Gerya, 2008).

7.3. Tectonic implications

The Astaneh rocks are typically formed of a medium to high-K calc-alkaline suite (Fig. 4c), in which quartz-diorites, granodiorites and monzogranites are the dominant rock types. Regarding field relations, petrography and geochemistry these rocks show similarities with intrusions in active continental margins. Furthermore, as discussed earlier, rocks of the Astaneh area are enriched in LILE such as Cs, K, Rb, and Th with respect to the HFSE, especially Nb and Ti (Figs. 5 and 6). Saunders et al. (1980) explained the high LILE abundances of continental calc-alkaline magmas as resulting from the presence of enriched mantle beneath continental margins. Magmas with these geochemical characters are generally ascribed to the subduction-related environments and the role of crustal source component in the genesis of these rocks (e.g. Rogers and Hawkesworth, 1989; Sajona et al., 1996). High Th/Yb ratios correlated with high values for La/Yb are consistent with continental arc magmas (Fig. 8c). In summary, the geochemical and mineralogical data of the Astaneh rocks indicate a subduction-related environment. These data are consistent with previous studies on the plutonic rocks in the Sanandaj–Sirjan Zone (Ahmadi Khalaji, 2006; Ahmadi-Khalaji et al., 2007; Arvin et al., 2007). Our results are in good agreement with the general model of Berberian (1983) and

Shahabpour (2005), which assumed that the Sanandaj–Sirjan calc-alkaline magmatic arc formed over a high angle subducting oceanic slab in the Neo-tethyan subduction zone during Late Triassic to Late Cretaceous time.

8. Conclusions

The Astaneh rocks belongs to metaluminous to slightly peraluminous, medium to high-K calc-alkaline series, and displays geochemical characteristics typical of volcanic arc granites related to an active continental margin. Two separate magmatic cycles have been identified. One is represented by diorites that form a part of the enclave population for which a primary origin from an enriched mantle source is proposed. The second cycle is more silicic. It is formed by Qtz-diorites and granodiorites, the most abundant rocks in the Astneh intrusion. An origin by partial or total melting of a composite source with amphibolites and sediments (subducted mélange) is proposed for this silicic magmatic cycle. Direct melting or fractionation from a diorite source is very unlikely.

9. Uncited reference

Castro et al. (2000). Q1

Annen, C., Blundy, J. D. & Sparks, R. S. J., 2006. The genesis of intermediate and silicic magmas in deep crustal hot zones. Journal of Petrology 47, 505-539.

References

Agard, P., Omrani, J., Jolivet, L., Mouthereau, F., 2005. Convergence history across Zagros (Iran): constraints from collisional and earlier deformation. International Journal of Earth Sciences 94, 401–419.

Ahmadi Khalaji, A., 2006. Petrology of the granitoid rocks of the Boroujerd area. Ph.D. Thesis, University of Tehran, Tehran, p. 190.

Ahmadi-Khalaji, A., Esmaeily, D., Valizadeh, M.V., Rahimpour-Bonab, H., 2007. Petrology and geochemistry of the granitoid complex of Boroujerd, Sanandaj–Sirjan Zone, Western Iran. Journal of Asian Earth Sciences 29, 859–877.

Alavi, M., 1994. Tectonics of the Zagros orogenic belt of Iran: new data and interpretations. Tectonophysics 229, 211–238.

Alavi, M., 2007. Structures of the Zagros fold-thrust belt in Iran. American Journal of Science 307, 1064–1095.

Amidi, S.M., Emami, M.H., Michel, R., 1984. Alkaline character of Eocene volcanism in the middle part of Central Iran and its geodynamic situation. Geologische Rundschau 73, 917–932.

Annen, C., Sparks, R.S.J., 2002. Effects of repetitive emplacement of basaltic intrusions on thermal evolution and melt generation in the crust. Earth and Planetary Science Letters 203, 937–955.

Arvin, M., Pan, Y.-M., Dargahi, S., Malekizadeh, A., Babaei, A., 2007. Petrochemistry of the Siah-Kuh granitoid stock southwest of Krman, Iran: implications for initiation of neotethys subduction. Journal of Asian Earth Sciences 30, 474–489.

Baharifar, A., 2004. Petrology of metamorphic racks in the Hamadan area. Ph.D. Thesis, Tarbiat Moalem University of Tehran, Tehran.

Berberian, M., 1983. Generalized tectonic map of Iran. In: Berberian, M., (Ed.), Continental Deformation in the Iranian Plateau. Geological Survey of Iran, Report No. 52, Tehran.

Berberian, F., Berberian, M., 1981. Tectono-plutonic episodes in Iran. In: Gupta, H.K., Delany, F.M. (Eds.), Zagros Hindukosh, Himalaya Geodynamic Evolution. American Geophysical Union, Washington, DC, pp. 5–32.

Berberian, M., King, G.C.P., 1981. Towards a paleogeography and tectonic evolution of Iran. Canadian Journal of Earth Sciences 18, 210–265.

Berberian, F., Muir, I.D., Pankhurst, R.J., Berberian, M., 1982. Late Cretaceous and early Miocene Andean-type plutonic activity in northern Makran and Central Iran. Journal of the Geological Society 139, 605–614.

Castro, A., Gerya, T.V., 2008. Magmatic implications of mantle wedge plumes: experimental study. Lithos 103, 138–148.

Castro, A., Stephens, W.E., 1992. Amphibole-rich polycrystalline clots in calc-alkaline granitic rocks and their enclaves. Canadian Mineralogist 30, 1093–1112.

Castro, A., Moreno-Ventas, I., De La Rosa, J.D., 1991. Multistage crystallization of tonalitic enclaves in granitoid rocks. Implications in magma mixing. Geologische Rundschau 80, 109–120.

Castro, A., Patiño Douce, A.E., Corretgé, L.G., de la Rosa, J.D., El-Biad, M., El-Hmidi, H., 1999. Origin of peraluminous granites and granodiorites, Iberian massif, Spain. An experimental test of granite petrogenesis. Contributions to Mineralogy and Petrology 135, 255–276.

Castro, A., Corretgé, L.G., El-Biad, M., El-Hmidi, H., Fernández, C., Patiño Douce, A.E., 2000. Experimental constraints on Hercynian Anatexis in the Iberian Massif, Spain. Journal of Petrology 41, 1471–1488. *[delete this reference]*

Chappell, B.W., White, A.J.R., 1974. Two contrasting granite types. Pacific Geology 8, 173–174.

De Paolo, D.J., 1981. A neodymiun and strontium isotopic study of the Mesozoic calc-alkaline granitic batholiths of the Sierra Nevada and Peninsular Ranges, California. Journal of Geophysical Research 86, 10470–10488.

Didier, J., Barbarin, B., 1991. Enclaves and Granite Petrology. Elsevier, Amsterdam.

Ghalamghash, J., Nédélec, A., Bellon, H., Abedini, M.V., Bouchez, J.L., in press. The Urumieh plutonic complex (NW Iran): a record of the geodynamic evolution of the Sanandaj-Sirjan zones – part I: petrogenesis and K/Ar

Ghiorso, M.S., Sack, R.O., 1995. Chemical mass transfer in magmatic processes. A revised and internally consistent thermodynamic model for the interpolation and extrapolation of liquid–solid equilibria in magmatic systems at elevated temperature and pressures. Contributions to Mineralogy and Petrology 119, 197–212.

Govindaraju, K., Potts, P.J., Webb, P.C., Watson, J.S., 1994. Report on Whin sill dolerite WS-S from England and Pitscurrie microgabbro PM-S from Scotland: assessment by one hundred and four international laboratories. Geostandard Newsletters 18, 211–300.

Hooper, R.J., Baron, I., Hatcher Jr., R.D., Agah, S., 1994. The development of the southern Tethyan margin in Iran after the break up of Gondwana: implications of the Zagros hydrocarbon province. Geosciences 4, 72–85.

Huppert, H.E., Sparks, S.J., 1988. The generation of granitic magmas by intrusion of basalt into continental crust. Journal of Petrology 29, 599–624.

Isacks, B., Barazangi, M., 1977. Geometry of Benioff Zones: lateral segmentation and downwards bending of the subducted lithosphere. Island arcs, deep sea trenches and back arc basins, Maurice Ewing Series 1, American Geophysical Union, pp. 99–114.

Kelemen, P.B., Hanghoj, K., Greene, A.R., 2003. One view of the geochemistry of subduction-related magmatic arcs, with emphasis on primitive andesite and lower crust. In: Rudnick, R.L. (Ed.), The Crust. Elsevier, Amsterdam, pp. 593–659.

Kretz, R., 1983. Symbols for rock-forming minerals. American Mineralogist 68, 277–279.

Leake, B.E., Woolley, A.R., Arps, C.E.S., Birch, W.D., Gilbert, M.C., Grice, J.D., Hawthorne, F.C., Kato, A., Kisch, H.J., Krivovichev, V.G., Linthout, K., Laird, J., Mandarino, J.A., Maresch, W.V., Nickel, E.H., Rock, N.M.S., Schumacher, J.C., Smith, D.C., Stephenson, N.C.N., Ungaretti, L., Whittaker, E.J.W., Youzhi, G., 1997. Nomenclature of amphiboles: report of the subcommittee on amphiboles of the International Mineralogical Association, Commission on new minerals and mineral names. Canadian Mineralogist 35, 219–246.

Lee, C.-T.A., Morton, D.M., Kistler, R.W., Baird, A.K., 2007. Petrology and tectonics of phanerozoic continent formation: from island arcs to accretion and continental arc magmatism. Earth and Planetary Science Letters 263, 370–387.

Martin, H., Smithies, R., Rapp, R., Moyen, J.F., Champion, D., 2005. An overview of adakite, tonalite–trondhjemite–granodiorite (TTG), and sanukitoid: relationships and some implications for crustal evolution. Lithos 79, 1–24.

Masoudi, F., 1997. Contact metamorphism and pegmatite development in the SW of Arak, Iran. Ph.D. Thesis, The University of Leeds, Leeds, p. 231.

Masoudi, F., Yardley, B.W.D., Cliff, R.A., 2002. Rb–Sr geochronology of pegmatites, plutonic rocks and a hornfels in the region southwest of Arak, Iran. Islamic Republic of Iran Journal of Sciences 13, 249–254.

Mazhari, S.A., Bea, F., Amini, S., Ghalamghash, J., Molina, J.F., Montero, P., Scarrow, J.H., Williams, I.S., 2009. The Eocene bimodal Piranshahr massif of the Sananadaj-Sirjan Zone, West Iran. A marker of the end of collision in the Zagros orogen. Journal of the Geological Society 166, 53–69.

Mohajjel, M., Fergusson, C.L., Sahandi, M.R., 2003. Cretaceous–Tertiary convergence and continental collision, Sanandaj–Sirjan Zone, Western Iran. Journal of Asian Earth Sciences 21, 397–412.

Montero, P., Bea, F., 1998. Accurate determination of 87Sr/86Sr and 143Sm/144Nd ratios by inductively coupled-plasma mass spectrometry in isotope geosciences: an alternative to isotope dilution analysis. Analytica Chimica Acta 358, 227–233.

Nakamura, N., 1974. Determination of REE, Ba, Fe, Mg, Na, and K in carbonaceous and ordinary chondrites. Geochimica et Cosmochimica Acta 38, 757–775.

Omrani, J., Agard, P., Whitechurch, H., Benoite, M., Prouteav, G., Jolivet, L., 2008. Arc-magmatism and subduction history beneath the Zagros Mountains, Iran: a new report of adakites and geodynamic consequences. Lithos 106, 380–398.

Patiño Douce, A.E., 1995. Experimental generation of hybrid silicic melts by reaction of high-Al basalts with metamorphic rocks. Journal of Geophysical Research 100, 15623–15639.

Patiño Douce, A.E. 1999. What do experiments tell us about the relative contributions of crust and mantle to the origins of granitic magmas? In: Castro, A., Fernandez, C., Vigneresse, J.L. (Eds.), Understanding Granites: Integrating New and Classical Techniques. Geological Society of London, Special Publication, 168, pp. 55–75.

Ratajeski, K., Sisson, T.W., Glazner, A.F., 2005. Experimental and geochemical evidence for derivation of the El Capitan Granite, California, by partial melting of hydrous gabbroic lower crust. Contributions to Mineralogy and Petrology 149, 713–734.

Rogers, G., Hawkesworth, C.J., 1989. A geochemical traverse across the North Chilean Andes: evidence for crust generation from the mantle wedge. Earth and Planetary Science Letters 91, 271–285.

Sabzehei, M., 1994. Geological Quadrangle Map of Iran, No. 12, Hajiabad, 1:250,000, Geological Survey of Iran.

Sabzehei, M., Majidi, B., Alavi-Tehrani, N., Etminan, H., 1970. Preliminary report, geology and petrography of the metamorphic and igneous complex of the central part of Neyriz Quardangle (compiled by Watters, W.A., Sabzehei, M.), Geological Survey of Iran. Internal Report, 60 p.

Sajona, F.G., Maury, R.C., Bellon, H., Cotton, J., Defant, M., 1996. High field strength elements of Pliocene–Pleistocene island-arc basalts Zamboanga Peninsula, Western Mindanao (Philippines). Journal of Petrology 37, 693–726.

Saunders, A.D., Tarney, J., Weaver, S.D., 1980. Transverse geochemical variations across the Antarctic Peninsula, implications for the genesis of calc-alkaline magma. Earth and Planetary Science Letters 46, 344–360.

Sengor, A.M.C., 1987. Tectonics of the tethysides. Annual Review of Earth and Planetary Sciences 15, 213–244.

Sengor, A.M.C., 1992. The palaeo-Tethyan suture: a line of demarcation between two fundamentally different architectural styles in the structure of Asia. Island Arc 1, 78–91.

Shahabpour, J., 2005. Tectonic evolution of the orogenic belt in the region located between Kerman and Neyriz. Journal of Asian Earth Sciences 24, 405–417.

Sisson, T.W., Ratajeski, K., Hankins, W.B., Glazner, A.F., 2005. Voluminous granitic magmas from common basaltic sources. Contributions to Mineralogy and Petrology 148, 635–661.

Stephens, W.E., 2001. Polycrystalline amphibole aggregates (clots) in granites as potential I-type restite: an ion microprobe study of rare-earth distributions (2001). Australian Journal of Earth Sciences 48, 591–602.

Stöcklin, J., 1968. Structural history and tectonics of Iran: a review. American Association of Petroleum Geologists Bulletin 52, 1229–1285.

Stöcklin, J., Setudinia, A., 1972. Lexique Stratigraphique International Volume III ASIE. Centre National de la Recherche Scientifique. 15, quai Anatole-France, 75 p (Paris-VII).

Sun, S.S., Mc Donough, W.F., 1989. Chemical and isotopic systematics of oceanic basalts: implications for mantle composition and processes. Geological Society, Special Publications, London 42, 313–345.

Tatsumi, Y., Shukuno, H., Sato, K., Shibata, T., Yoshikawa, M., 2003. The Petrology and Geochemistry of high-magnesium andesites at the Western Tip of the Setouchi Volcanic Belt, SW Japan. Journal of Petrology 44, 1561–1578.

Thompson, A.B., Matile, L., Ulmer, P., 2002. Some thermal constraints on crustal assimilation during fractionation of hydrous, mantle-derived magmas with examples from Central Alpine Batholiths. Journal of Petrology 43 (3), 403–422.

Valizadeh, M.V., Cantagrel, J.M., 1975. Prèmieres données radiométricques (K–Ar et Rb–Sr) sur les micas du complexe magmatique du Mont Alvand. Près Hamadan (Iran occidental). Comptes Rendus des Seances de l'Academie des Sciences. Series D 281, 1083–1086.

Vernon, R.H., Paterson, S.R., 2002. Igneous origin of K-feldspar megacrysts in deformed granite of the Papoose Flat Pluton, California, USA. Electron Geoscience (Published online, 16 July 2002).

Winther, K.T., Newton, R.C., 1991. Experimental melting of hydrous low-K tholeiite: evidence on the origin of Achaean cartons. Bulletin Geological Society of Denmark 39, 213–228.

Wyllie, P.J., 1984. Constraints imposed by experimental petrology on possible and impossible magma source and products. Transactions of the Royal Society of London 310, 439–456.